Development of an Efficient Hybrid Energy Storage System (HESS) for Electric and Hybrid Electric Vehicles

by

Kun Zhuge

A thesis
presented to the University of Waterloo
in fulfillment of the
thesis requirement for the degree of
Master of Applied Science
in
Electrical and Computer Engineering

Waterloo, Ontario, Canada, 2013

AUTHOR'S DECLARATION

I hereby declare that I am the sole author of this thesis. This is a true copy of the thesis, including any required final revisions, as accepted by my examiners.

I understand that my thesis may be made electronically available to the public.

ABSTRACT

The popularity of the internal combustion engine (ICE) vehicles has contributed to global warming problem and degradation of air quality around the world. Furthermore, the vehicles' massive demand on gas has played a role in the depletion of fossil fuel reserves and the considerable rise in the gas price over the past twenty years. Those existing challenges force the auto-industry to move towards the technology development of vehicle electrification. An electrified vehicle is driven by one or more electric motors. And the electricity comes from the onboard energy storage system (ESS). Currently, no single type of green energy source could meet all the requirements to drive a vehicle. A hybrid energy storage system (HESS), as a combination of battery and ultra-capacitor units, is expected to improve the overall performance of vehicles' ESS. This thesis focuses on the design of HESS and the development of a HESS prototype for electric vehicles (EVs) and hybrid electric vehicles (HEVs).

Battery unit (BU), ultra-capacitor unit (UC) and a DC/DC converter interfacing BU and UC are the three main components of HESS. The research work first reviews literatures regarding characteristics of BU, UC and power electronic converters. HESS design is then conducted based on the considerations of power capability, energy efficiency, size and cost optimization. Besides theoretical analysis, a HESS prototype is developed to prove the principles of operation as well. The results from experiment are compared with those from simulation.

ACKNOWLEDGEMENTS

Upon the completion of the thesis, please allow me to express my deepest gratitude to my supervisor, Dr. Mehrdad Kazerani, although I will never thank him enough for his continuous support, as an old Chinese saying that “for one day as my teacher, for ever I respect him as my parent.” During the past two years, I felt fortune enough to be the student of such a patient, encouraging and knowledgeable supervisor. Talking with him was always wonderful experience to light me up. His caring and inspiration gave me confidence and lots of fresh ideas to improve my research work, which would not have been possible without his help. I would like to thank Dr. Amir Khajepour and Dr. Kankar Bhattacharya, for attending my graduate seminar and providing valuable suggestions to improve my thesis quality.

I appreciate the funding from ORF and APC, the support from Dr. Khajepour, to give me a chance to get involved into the project with GM as an industry partner for research.

In particular to my beloved Yifei, I am forever grateful to your understanding and insisting. Despite of being apart temporally, my life is still enriched by sharing success and setbacks with you. I also want to extend my gratefulness to my family, for their endless love to me and unconditional supporting.

I wish to thank my partner Noreen for the friendship and her words of encouragement. Likewise thanks to Amir and Yong for bringing knowledge and happiness to our office. Thanks to Jess and Neil for help in and outside classrooms. Thanks to Qiang and Chong for their caring. Thanks to Fei, Fred, Shi, Kevin and Duanmu, my fellows from “504A”, for making me feel at home during my study in Canada. And thanks to all the help from all my friends when it is most required during my graduate study.

I dedicate this thesis to my parents and my love, Yifei.

TABLE OF CONTENTS

LIST OF FIGURES

LIST OF TABLES

Chapter 1

Introduction

1.1 Motivation

The popularity of vehicles has brought great convenience to our lives in the modern society. However, the nature of traditional vehicles that are powered by the internal combustion engine (ICE) has created serious environmental crises like global warming and degradation of air quality. These problems have drawn considerable attention from the governments and the public. The US president together with other 7 leaders of G8 countries announced the goal to limit global temperature rise to 2 degrees Celsius by 2030 at the G8 Summit in July, 2009 [1]. Consequently, stricter exhaust gas regulations such as EU5 and EU6 have been established to force auto manufactures to invest in vehicles powered by renewable sources of energy. The rising public awareness of environmental challenge is a drive behind the ongoing technical developments. One market research of electric vehicle has exposed that people who know about electric vehicle are willing to buy one if “electric vehicles offer the same convenience and value as conventional vehicles” [2]. This phenomenon makes auto manufactures willing to contribute more in the development of new technologies in the areas of electric vehicles (EVs) and hybrid electric vehicles (HEVs).

The increase in the number of vehicles leads to massive demand on gas coming from crude oil. As a survey performed by IBM shows, three quarters of U.S. oil needs are for transportation [2]. The finite and uncertainty of oil reserves has resulted in considerable

rise in the price of gas over the past twenty years, a trend that is expected to continue in the near future [3]. So the need of renewable energy sources for transportation is evident.

One of the most practical and competitive solutions is to electrify vehicles. One report from California Environmental Protection Agency's Air Resources Board has implied that range of an EV is three times longer than that of a gasoline powered vehicle if given the same amount of fuel energy [2]. Besides efficiency, electricity can be easily accessed nowadays and there are multiple renewable energy sources for electricity generation such as wind and solar farms, and hydro generation [4].

EV is not a new concept. Earlier, at the beginning of the twentieth century, there were more EVs than the gasoline-powered vehicles in the United State. Unfortunately, the latter option began to dominate the market due to the limitation of an energy storage system with high specific energy and high specific power for EVs. Right now, revival of EVs has seen its opportunities upon the considerable battery technology developments, accompanied by challenges of global warming and oil price spike.

1.2 Background on EVs and HEVs

Electrification of vehicles results in the birth of EVs and HEVs, which are driven by one or more electric motors and powered by electricity. The electricity for an EV or HEV comes from either an external power supply, like trolley buses, or an internal energy storage system. Focus of this thesis is on the internal energy storage system (ESS) for EVs and HEVs.

Categorized by the mechanical connections, series topology and parallel topology are the basic two structures used for the Hybrid Electric Vehicle (HEV) powertrains [5], [6]. In a series structure, the entire propulsion power is provided through electric motors. Among the different types of energy sources, battery pack is the most important one that give

power to electric motors. Other examples can be a range extender, the integration of a generator with an ICE operating at its most efficient point [1], [6], such as Chevrolet Volt from GM or an on-board Fuel Cell engine [7]. In a parallel structure, an ICE and an electric motor are coupled mechanically to provide wheels with requested speed and torque [5]. This implies a smaller electric motor than the traction motor in the series structure. But, on the other hand, more advanced control techniques should be implemented for the hybrid system. An additional type of topology is derived from the combination of the two structures mentioned above, namely parallel/series topology, with increasing flexibility of operation [5]. A good example from this group is the Toyota Prius.

In order to represent the level of hybridization directly and clearly, Reference [5] offers the concept of hybridization factor (HF),

$$HF = \frac{P_{EM}}{P_{EM}+P_{ICE}} \tag{1.1}$$

where P_{EM} and P_{ICE} are the components of power supplied by the electric motor and internal combustion engine, respectively. As a results, the minimum value HF=0 represents an IC engine vehicle, while the maximum value HF=1 represents a pure EV. The vehicles with HF values between 0 and 1 are hybrid electric vehicles (HEVs). Figure 1.1 gives classifications of the most recent products in industry based on HF [5].

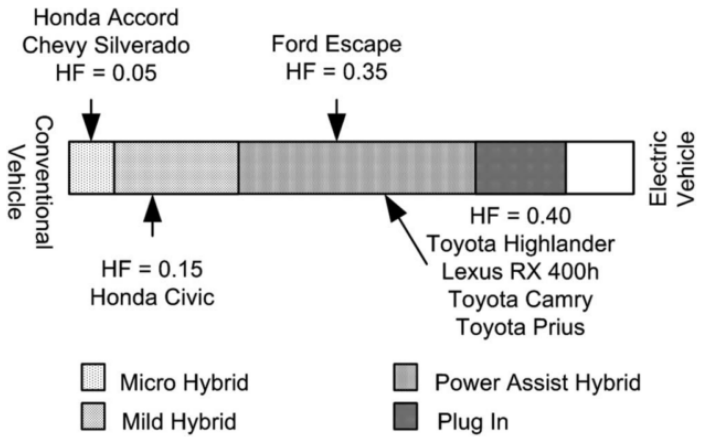

Figure 1-1 Classifications of Recent Vehicles Based on HF [5]

EVs and HEVs should be refillable when the energy is used up. Those with a rechargeable battery pack are called plug-in electric vehicles (PEVs) and plug-in hybrid electric vehicles (PHEVs). A battery charger connects the battery pack with the electrical grid. Therefore, PEVs and PHEVs can be easily charged to full capacity at home or in a charging station. Many auto manufactures have released their PEV or PHEV version of commercial passenger cars by the end of 2012, like Porsche Panamera S E-Hybrid, Volvo V60 Plug-in Hybrid, and Honda Accord Plug-in Hybrid. Tesla Model S is a pure electric vehicle, belonging to PEV group and it can be charged for 208 miles within 30 minutes by Tesla's supercharger [8].

1.3 Research Objectives

Transportation electrification will lead to massive demand on a high-performance and efficient ESS for PEVs and PHEVs. The research reported in this thesis examines the possibility of a hybrid energy storage system (HESS), as a combination of lithium-ion batteries and ultra-capacitors, for PEVs and PHEVs. To have an experimental verification of the capabilities of the proposed HESS, a lab prototype is built in laboratory and the simulation and experimental results are analyzed and comparatively evaluated.

1.4 Organization of the Thesis

This thesis is made up of five chapters and two appendices. Chapter 1 explains the significance of vehicle electrification and provides basic knowledge of EVs and HEVs. Chapter 2 is a technical survey of the state-of-the art in EV field and a literature review on the main components. Chapter 3 presents the design process of HESS based on the available power electronic converter technologies and control techniques. The designed circuit is simulated using PSIM simulation package and studies the integration of HESS with a Tesla Model S. Chapter 4 records the process of implementation of HESS prototype in laboratory and makes a comparison between the simulation and experimental results. Chapter 5 makes conclusions based on the study reported in the thesis and suggests some items for future work. Appendix A is a table listing the specifications of Tesla Model S that will be used for theoretical analysis of HESS. In Appendix B, hardware components of HESS prototype has been described in detail.

Chapter 2

Literature Review

2.1 Vehicle Power Requirement

The United States Environmental Protection Agency (EPA) has developed a variety of vehicle drive schedules to represent typical vehicle patterns. These include: New York City Cycle (NYCC) to describe low-speed stop-and-go city traffic condition, US06 to describe high-acceleration aggressive driving schedule, Highway Fuel Economy Driving Schedule (HWFET) to describe highway driving conditions under 60mph, and UDDS (commonly called LA4) to describe city driving conditions [9].

From these drive cycles, acceleration or deceleration of a vehicle at any moment can be found from the difference between the vehicle speeds at two successive moments. Therefore, corresponding power usage of a vehicle can be calculated if additional parameters of a tested vehicle are given. These parameters include mass, aerodynamic drag, rolling resistance, gear ratio and transmission efficiency. Road grade data is not coupled with drive cycle: thus, information on the road grade is needed to produce a complete power profile for a vehicle over a drive cycle. The process of deriving the required power can be formulated as follows [4].

Physical analysis illustrates that the power (W) at a vehicle's wheel is the product of wheel torque (Nm) and its angular speed (rad/s).

$$Power = Torque * \omega \quad (2.1)$$

The vehicle's wheel torque is the product of equivalent force $Force_{eq}$ (N) on the wheel and wheel's radius r (m).

$$Torque = Force_{eq} * r \tag{2.2}$$

Based on Newton's law of motion, the equivalent force on the wheel can be calculated as the sum of force components due to aerodynamic drag, F_{ad} (N), vehicle's acceleration/deceleration, F_{ac} (N), rolling resistance, F_{rr} (N), and gravity, F_g (N).

$$Force_{eq} = F_{ad} + F_{ac} + F_{rr} + F_g \tag{2.3}$$

The aerodynamic drag is given by equation (2.3). In this expression, C_{ad} is the drag coefficient determined by vehicle's body shape, A (m^2) is the frontal area, ρ is the density of air and v represents vehicle velocity. The combination of C_{ad} and A is called "drag area" because drag will be reduced if the frontal area reduces [4][10].

$$F_{ad} = \frac{1}{2} * \rho v^2 C_{ad} A \tag{2.4}$$

Newton's second law of motion tells us that the net force acting on a body is proportional to the acceleration of the body. In equation (2.5), m (kg) is mass of the vehicle and a (m/s^2) is vehicle's acceleration.

$$F_{ac} = ma \tag{2.5}$$

Rolling resistance is another kind of drag because of the friction between the road and vehicle's tire. In equation (2.6), g is the gravitational acceleration and C_r is the rolling resistance coefficient, whose value is variable due to the differences between the materials of the road and tire. Typical value of C_r for a vehicle running on concrete road is between 0.01 and 0.015.

$$F_{rr} = C_r mg\cos\theta \tag{2.6}$$

Gravitational resistance is caused by the slope (grade) of the road. In equation (2.7), θ is the angle between the road surface and the horizontal plane.

$$F_g = mgsin\theta \tag{2.7}$$

Angular speed can be derived from vehicle velocity v or calculated based on the motor speed n (rpm) and gear ratio C_{gr}.

$$\omega = \frac{v}{r} = \frac{n}{C_{gr}60} * 2\pi \tag{2.8}$$

No energy loss is taken into consideration in the above formulations. However, the study of electric vehicle would become meaningless if the energy transfer efficiency from vehicle's engine to wheel is not taken into account. Actually, this number is as low as 30%. VTW (vehicle to wheel) efficiency is defined to represent efficiency of the energy transfer process [11]

$$VTW = \frac{E_{out}}{E_{in}} = \frac{E_{wheel}}{E_{fuel}+E_{grid}} \tag{2.9}$$

where E_{wheel}, E_{fuel} and E_{grid} are the energy received at the wheel, the energy supplied from the fuel via ICE and the energy received from the grid for charging the batteries, respectively. VTW efficiency for a conventional vehicle is less than 30% while for an electric vehicle it goes up to 78%. In this thesis, the VTW efficiency for EV is assumed to be equal to:

$$\gamma = 78\%$$

Case study for Tesla

Appendix A lists the available parameters for Tesla Model S (85P). Assuming that a Tesla sedan is running on UDDS drive cycle, shown in Figure 2-1, and Tesla Model S' parameters will produce the corresponding power curve shown in Figure 2-2.

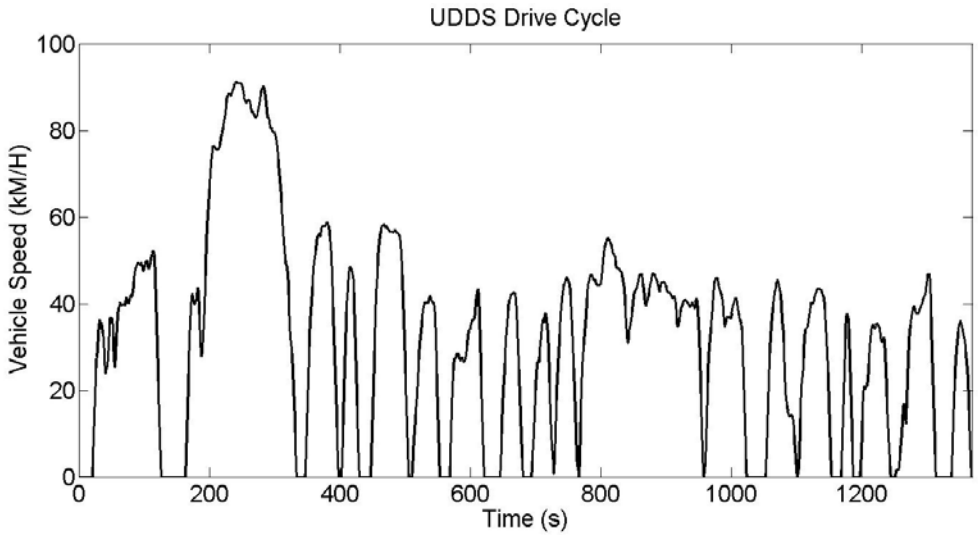

Figure 2-1 UDDS Drive Cycle

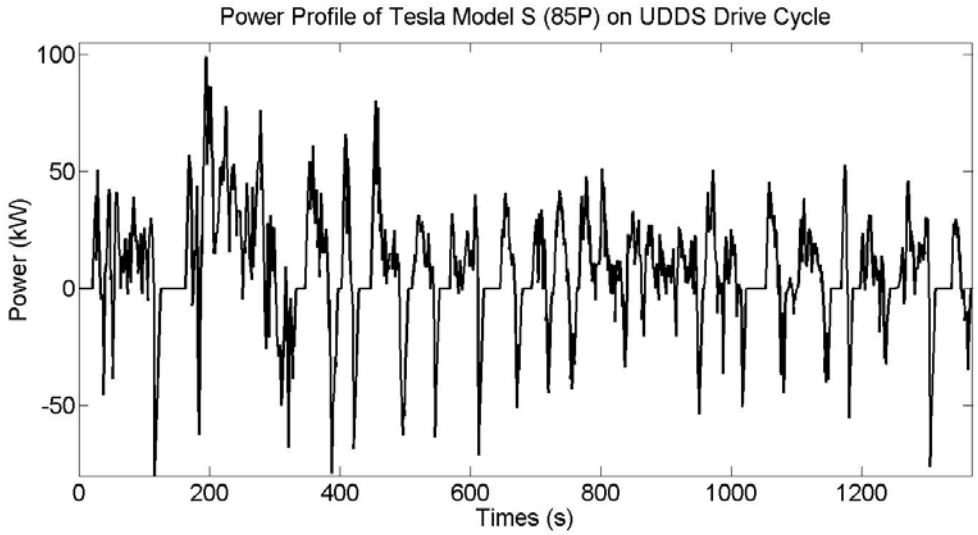

Figure 2-2 Calculated Power Profile of Tesla Sedan on UDDS Drive Cycle

2.2 EV Powertrain Technologies

Electric powertrain of an EV or HEV is made up of three key components: an electric motor, a power electronic converter and an ESS.

2.2.1 Electric Motors

Electric motors (EMs) have a crucial advantage over ICEs due to the fact that an EM is able to produce its maximum torque at very low shaft speeds. The maximum torque will be kept constant as the motor shaft speed is increased until the maximum motor power is reached. After that moment, the motor torque will reduce gradually as the shaft speed continuously goes up. Figure 2-3 shows a typical relationship between electric motor torque and power with respect to shaft speed in comparison with the torque of a 6-cylinder high-performance IC engine [12].

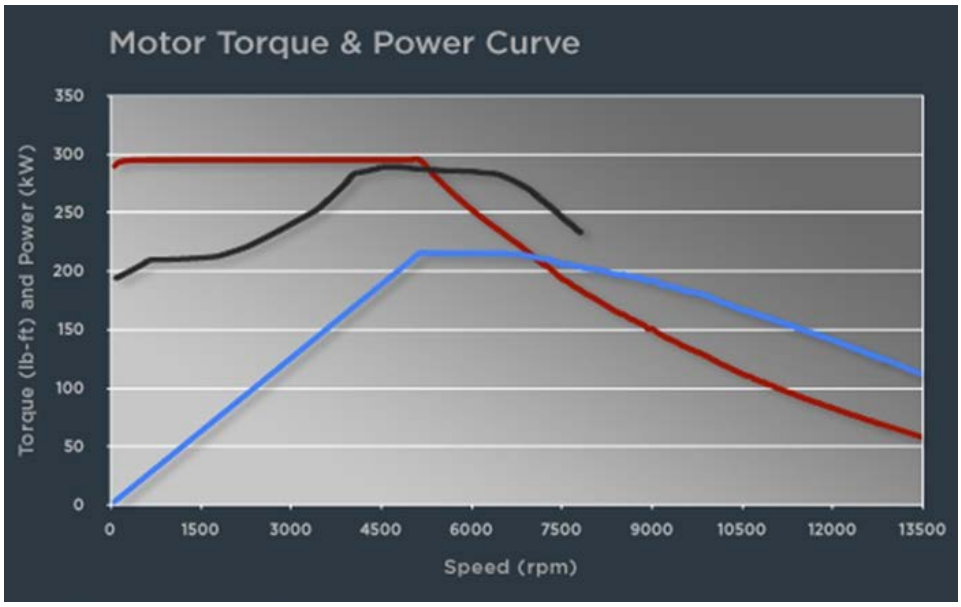

Figure 2-3 Torque & Power Versus Speed Characteristics of an Electric Motor and an IC Engine [12]

Among types of electric motors, the DC motor has the simplest structure and simplest controller. The characteristics of a DC motor always make it a candidate for conducting experiments in the laboratory. However, DC motors won't be taken into consideration for application of electric vehicle in industry due to their low efficiency, heavy weight, high maintenance requirements and safety issues [1].

Instead, induction motors (or AC asynchronous motors) are by far the most popular type of electric motors in industry due to their low cost, high power and torque in a small, lightweight package that make them attractive for EV application. Permanent magnet synchronous motors (PMSMs) are another type of well-known electric motors with even higher torque per input unit power than induction motors. But higher cost of PMSMs (due to limited rare earth materials) makes them less popular than induction motors.

Each electric motor comes with a motor driver, which is similar to an ICE management system. For DC motors, a driver is a DC/DC converter. In the case of AC motors, the drivers will be DC/AC converters (inverters) providing motors with the necessary voltage at the required frequency. Because of this, ESS will be connected with the input of motor drivers and the design of ESS should respect the limitations of electric motor drivers.

2.2.2 Energy Storage Device

2.2.2.1 Types of Energy Storage Devices for EV and HEV

For EVs and HEVs, ESS acts as power and energy source for vehicle propulsion. The acceleration performance is determined by the maximum power from ESS while the range of the vehicle is determined by the energy capability of ESS. The criterion for evaluation of an ESS consists of energy density, power density, cost, lifetime and maintenance requirements [13]. Reference [13] gives a comprehensive review of the state-of-the-art ESS with different types of energy storage devices.

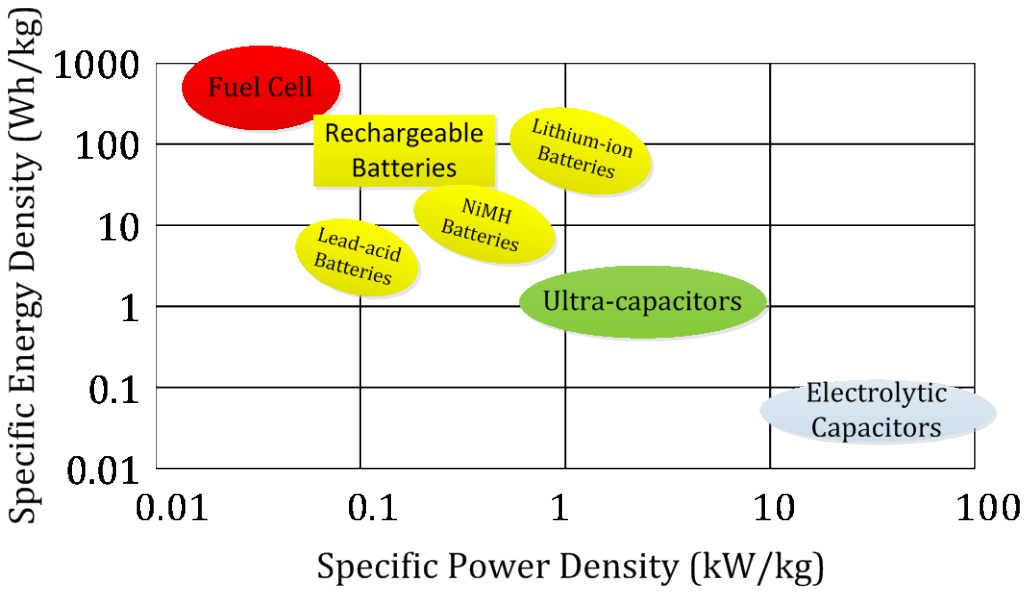

Figure 2-4 Specific Power and Specific Energy of Different Types of Energy Storage Device

Figure 2-4 compares the specific power and specific energy of fuel cell, rechargeable batteries, super-capacitors and electrolytic capacitors.

Fuel cell is an energy source with zero emissions. However, the extremely low power capability makes it impractical for vehicle application despite of its high energy density. Rechargeable batteries have recently become widespread energy storage devices as a result of their relatively high energy density, compact size and reliability. Among rechargeable batteries, lead-acid battery adopts the oldest but the most mature technology and has been around for more than 100 years. However, both energy and power densities of lead-acid batteries are relatively low. Nickel-Metal Hydride (NiMH) batteries have twice the energy density of lead-acid batteries and are friendly to environment. The drawbacks of NiMH batteries are reduced cycle life for high discharging current and memory effects [5], [13], [14].

Lithium-ion batteries are a promising technology with desirable characteristics in terms of low memory effect, high specific power of over 1000W/kg, high specific energy of over 100Wh/kg, and long battery cycle life of over 1000 with current technology [13]. The success of Tesla is a strong proof that lithium-ion batteries are powerful enough for EV applications.

Ultra-capacitors (or super-capacitors) are non-chemical energy storage. The positive and negative charges are physically stored on two parallel plates of very large surface area with an insulator in the middle. That is why ultra-capacitors are capable of very high specific power. The cycle life of ultra-capacitor can exceed 1million. The technical problem with ultra-capacitors is their low energy density [5], [13].

Since no single energy storage device at the present stage of technology can meet all the requirements imposed by road vehicles, it is worth trying to combine different types of energy storage devices to improve the overall performance of ESS.

2.2.2.2 Lithium-Ion Battery Model

An accurate lithium-ion battery model is of significance for circuit design and simulation because it would help in predicting or optimizing the circuit performance prior to implementation. Currently, a variety of battery models with different degrees of complexity exist. Among these, a comprehensive electrical battery model has been proposed in [15], [16] which is compatible with lead-acid, NiMH, Li-ion and polymer Li-ion batteries. As shown in Figure 2-5, there are two parts in the battery model. The first part on the left-hand side represents battery lifetime as capacity of battery drops based on accumulated cycle number. On the right hand side, the RC network takes advantage of Thevenin-based battery model. However, all the parameters are functions of state-of-charge (SoC) of the battery. The most important non-linear relationship between open-circuit voltage and SoC is also provided in [15]. As a result, the proposed battery model

produces a fully simulation-compatible model by combining lifetime prediction, steady state, accurate transient response and dynamic performance. The parameters used in the model can be extracted by introducing a special procedure. Finally, it is claimed in the paper that the battery model accurately predicted lithium-ion battery lifetime with 2% variation and voltage within an error of 30mV when the battery SoC is varied from 10% to 100%.

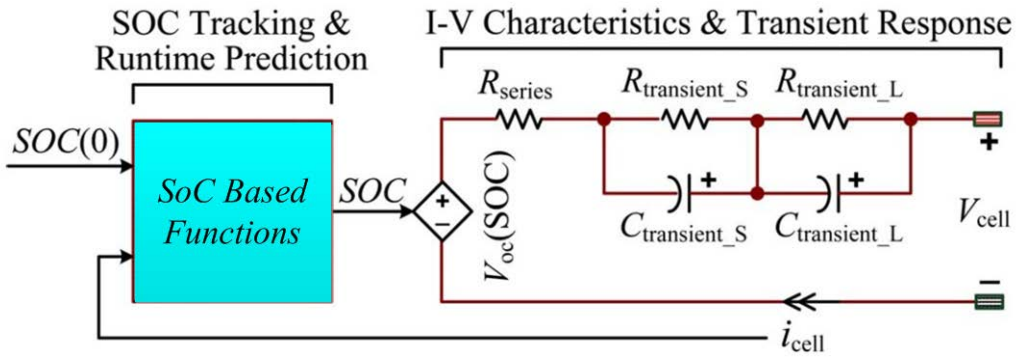

Figure 2-5 An Accurate Electrical Battery Model [16]

2.2.2.3 Ultra-capacitor Model

Similar to battery, ultra-capacitor needs an electrical model to be used in simulation for circuitry design. Research work in [17] applied the electrochemical impedance spectroscopy (EIS) technique on Maxwell BCAP0010 ultra-capacitor to extract 14 RLC parameters in its electrical model. The characteristics of the ultra-capacitor used are similar to those of the ultra-capacitors used in the tests reported in this thesis. Therefore, the ultra-capacitor model produced in PSIM in this thesis is derived from [17].

In the model, as shown in Figure 2-6, four parts are put together to describe ultra-capacitor behavior for automotive application. For ultra-capacitor capacitance, part of it has a linear relationship with the voltage and part of it keeps constant in value. “Circuit 1” is going to consider electrolyte ionic resistance temperature dependence in low

frequency range. The value of capacitance will increase in average frequency range due to the existence of “Circuit 2”. Leakage current and internal charge redistribution can be determined from the resistor and capacitor combination in “Circuit 3”.

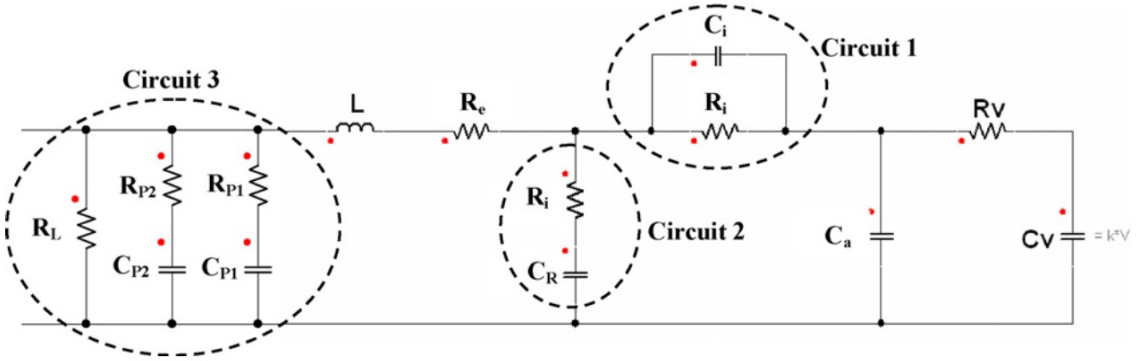

Figure 2-6 Ultra-capacitor Model [17]

2.2.2.4 Equivalent RLC Networks Impedance

Using accurate models of individual battery and ultra-capacitor cells to simulate an ESS with a large number of series and parallel-connected battery and ultra-capacitor cells is practically impossible due to the limitation of computer memory and processor speed, or the simulation time will be very long. This problem has been noticed by other researchers and has forced them to derive equivalent impedances for series-parallel RC networks based on Laplace Transform [18].

For a string of parallel RC networks shown in Figure 2-9, the equivalent resistance is equal to n times of individual cell resistance and the equivalent capacitance is equal to individual cell capacitance divided by n.

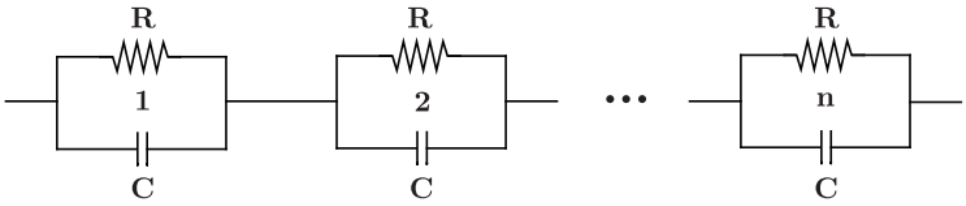

Figure 2-7 Series RC Network

For parallel connection of parallel RC networks shown in Figure 2-10, the equivalent resistance is equal to individual cell resistance divided by m and the equivalent capacitance is equal to m times of individual cell capacitance.

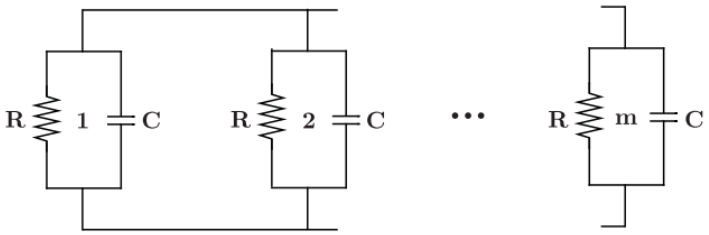

Figure 2-8 Parallel RC Network

As a result, for a series-parallel connected RC network, assuming it consists of n x m battery cells, the equivalent resistance is equal to n/m times individual cell resistance and the equivalent capacitance is equal to m/n times individual cell capacitance.

The equivalent inductance can be also derived by application of the method described above.

It is concluded that for a series-parallel connected RLC network, the equivalent resistance is equal to n/m times individual cell resistance, the equivalent inductance is equal to n/m times individual cell inductance, and the equivalent capacitance is equal to m/n times individual cell capacitance.

For a string of series connected battery cells, the equivalent open-circuit voltage is n time of individual battery cell voltage; for a number of parallel connected battery cells, the equivalent open-circuit voltage is equal to individual battery cell voltage.

Deriving of an ultra-capacitor pack model for simulation is similar to that for battery pack.

2.2.3 Cell balancing

Cell balancing is very important for both lithium-ion battery pack and ultra-capacitor pack because cell balancer can significantly prolong battery cell or ultra-capacitor cell cycle life and improve safety. There are two different balancing methods: passive and active. In passive balancing method, resistors are usually used to discharge the most charged cell. Implementation of this method is easy but this approach is energy lossy. Lithium-ion battery pack can only work with active balancing method because lithium-ion battery cells should be protected against over-charging/discharging and tightly controlled within the temperature-safe zone [19]. Many active balancing methods have been developed for lithium-ion battery pack. References [20] and [21] offer a novel configuration featuring low cost, high current capability and high efficiency.

2.2.4 Power Electronics Converter

The last component for EV powertrain is power electronic converter. Power electronic converters are located everywhere in the EV powertrain system. It acts as the power and energy manager of the system. For example, a battery balancing circuit equalizes the SOC of lithium-ion battery cells; an electric motor driver controls speed or torque and inverts DC voltage and current to the AC form for an AC motor; an on-board battery charger recharges the battery using the energy from the grid. Focus of this thesis will be

the DC/DC converter between lithium-ion battery pack and ultra-capacitor pack, as an integral part of the HESS for EVs or HEVs.

Batteries and ultra-capacitors are all DC energy sources but with a huge difference in terms of power and energy capabilities because of the different types of internal reactions. Lithium-ion battery has high specific energy while ultra-capacitor has high specific power density. Therefore, it is expected that ESS overall performance can be improved by appropriate combination of battery and ultra-capacitor in the design of HESS. In the recent years, many topologies for HESS have been proposed, but all of them have their pros and cons [13], [14], [22], [23].

The simplest topology, shown in Figure 2-9(a), is based on direct connection of battery and ultra-capacitor packs across the DC bus. No DC/DC converter and controller are needed for the hybrid system. This topology is very easy to implement and results in cost reduction. The disadvantage is that ultra-capacitor module cannot be fully utilized because the voltage of ultra-capacitor module is clamped by the battery voltage.

The HESS topologies equipped with DC/DC converters can be categorized into two groups: partially-decoupled configuration and fully-decoupled configuration. In partially-decoupled configurations, shown in Figures 2-9(b) and (c), either battery pack or ultra-capacitor pack is directly connected to the DC bus. When battery is connected to the dc bus directly (Figure 2-9(c)), UC can operate in a wide range of terminal voltage due to the presence of DC/DC converter. However, in this case, BU is exposed to fast-changing charging/discharging currents due to fast changes in the torque and power of the motor. Another drawback of this configuration is the relatively larger size of DC/DC converter as a result of peak power handling responsibility of UC.

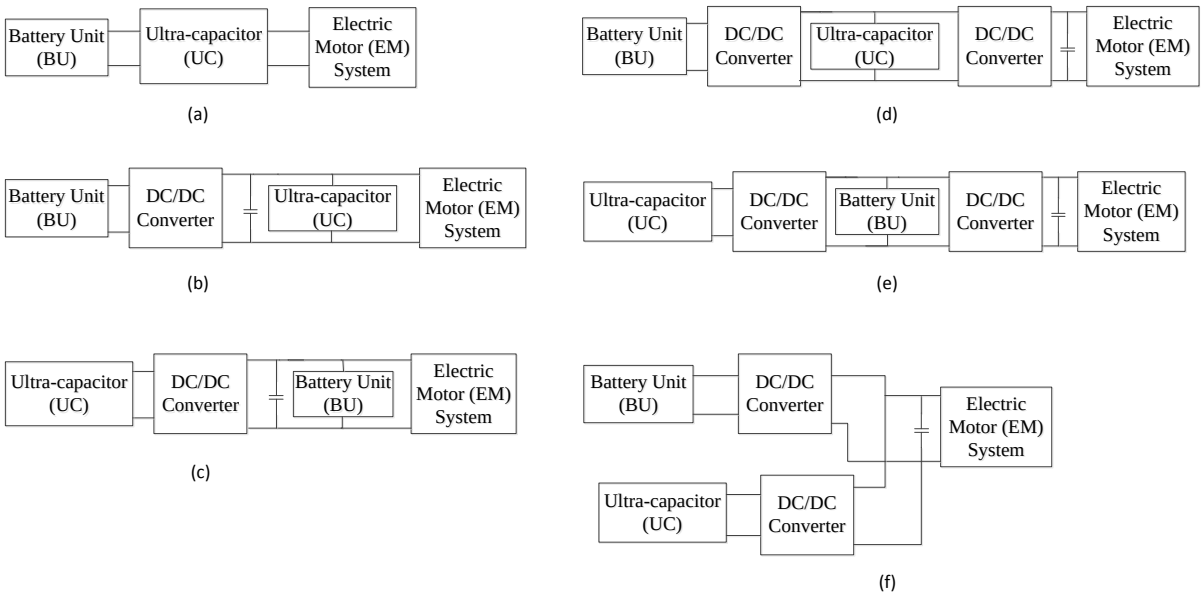

Figure 2-9 HESS Topologies

When UC is connected to the DC bus directly (Figure 2-9(b)), the power from BU is controlled by DC/DC converter. Fast changes in the power during acceleration or regenerating braking is handled by UC. This method might be more efficient to use; however, voltage of UC will fluctuate seriously due to UC's low energy density. Therefore, the DC bus will also experience high voltage variations, which seriously affects the operation of electric motor.

In fully-decoupled configuration, DC bus is immune to fluctuations of voltage as a result of using power electronic converter(s). Figures 2.9(d), (e), (f) present three main topologies in this category. In the configurations shown in Figures 2-9(d) and (e), BU and UC are cascaded. The use of high power level DC/DC converter makes this scheme economically unattractive.

The configuration shown in Figure 2-9(f) represents the most complete configuration of HESS by far. The DC/DC converter for BU will protect the battery from high frequent

charging/discharging current and the DC/DC converter for UC will help to increase the voltage range of UC towards its full utilization. At the same time, DC bus voltage will keep constant by cooperation of the two DC/DC converters. The disadvantage of this configuration is the higher cost, weight and volume, when compared with the previous topologies.

Chapter 3

Design of HESS

The design of HESS is conducted through analysis and its operation is verified by simulation and experiments. In simulation, a HESS designed based on the requirements of a full size vehicle will be used to prove the principles of operation. As a power profile has been derived for Tesla Model S on UDDS drive cycle, all of the simulations will use the available parameters of Tesla EV which are listed in Appendix A.

3.1 HESS topology selection

Pros and cons of different types of HESS topologies were reviewed in Chapter 2. The partially-decoupled HESS topology with ultra-capacitor unit (UC) directly connected to the DC bus, shown in Figure 3-1, is considered to be the most promising configuration for HESS application by comparison. There are several crucial reasons for this preference. Firstly, UC can be used more effectively. The energy stored in UC can be calculated by the equation (3.1) below:

$$E_{UC} = \frac{1}{2} C V_{UC}^2 \tag{3.1}$$

Thus, the percent usable energy of UC, or depth of discharge (DoD) [24], becomes a function of UC voltage:

$$DoD_{UC} = \frac{V_{initial}^2 - V_{min}^2}{V_{initial}^2} \times 100\% \tag{3.2}$$

For example, 50% UC voltage variation implies 75% available energy. Because of this, the topology in which BU and UC are connected directly is not an option for HESS due to clamped UC voltage. Secondly, fully-decoupled topology brings extra cost due to a second DC/DC converter, as well as extra weight and volume to the on-board energy storage system. Thirdly, comparison of the results obtained from the two structures in partially-decoupled group illustrates that the preferred topology is the one which is capable of protecting battery from fast-changing charging/discharging current and has a relatively smaller size of converter. In summary, HESS topology in Figure 3-1 is going to be the configuration of choice for the study reported in this thesis.

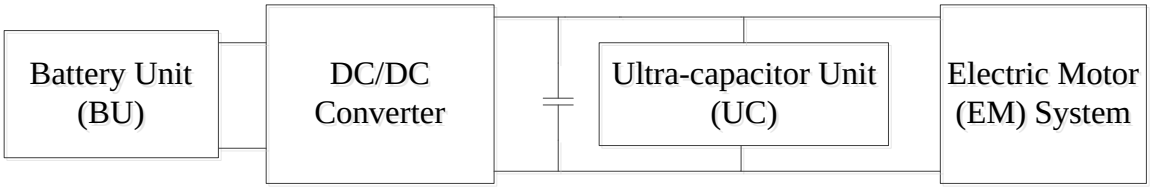

Figure 3-1 Partially-decoupled HESS Topology with UC Directly Connected to DC Bus

3.2 Design of DC/DC Converter

3.2.1 Bidirectional Buck-Boost Converter

Generally, ultra-capacitor is connected to high-voltage DC bus. It implies that the voltage selected for BU is lower than the voltage selected for UC. Therefore, the BU is connected to the low-voltage side of the DC/DC converter interfacing BU and UC. This structure has several advantages over the structure in which BU is connected to the high-voltage side of the DC/DC converter. First, a higher DC bus voltage reduces the current drawn by the inverter of traction motor for a given amount of power. The overall efficiency will be improved due to the fact that electrical power loss is a combination of current and resistance, $P_{loss} = I^2R$ [25]. Second, high voltage level of a battery pack translates into a large number of battery cells. As the number of battery cells goes up, imbalance problem becomes extremely serious by an exponential rate [14], [19]. Because of this, BU should

be placed on the lower voltage side of the DC/DC converter. UC also needs cell balancing techniques to equalize individual cell's performance. But due to the nature of UC (no chemical reaction), it is much easier to balance UC cells than BU cells. As a result, connection of the BU to the low-voltage side and UC to high-voltage side of the DC/DC converter minimizes the total cost for HESS cell balancing.

Among the bidirectional DC/DC converters, the simplicity of buck-boost converter makes it the first candidate, having in mind that the most important considerations for HESS, beside operational performance, are the weight and volume. Figure 3-2 shows the schematic diagram of a buck-boost converter.

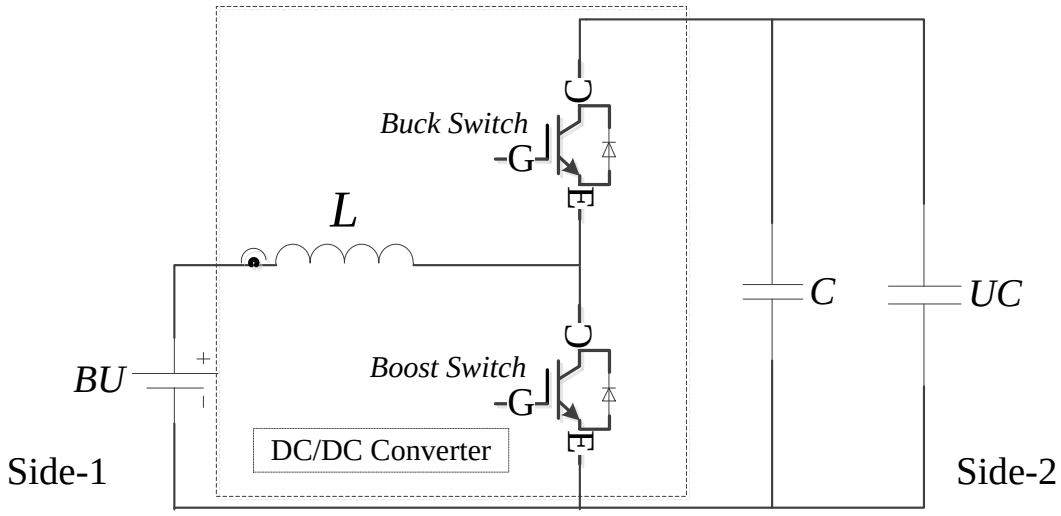

Figure 3-2 Bi-directional Buck-boost Converter

In the bi-directional buck-boost converter shown in Figure 3-2, the top switch is "buck switch" and the bottom one is "boost switch". When the power is flowing from side-1 to side-2, the boost switch is operating; when the power is flowing from side-2 to side-1, the buck switch is operating.

The next step is to calculate the value of inductance following textbook procedures [26], given DC/DC converter design criteria in Table 3-1.

The relationship between the current ripple and inductance of the inductor is expressed in the equation:

$$\frac{\Delta I}{I_L} = \frac{V_1(V_2 - V_1)}{f V_2 L} \leq 20\% \tag{3.3}$$

Based on the specifications in given in Table 3-1, the inductance of the inductor for HESS turns out to be $L \geq 121.46uH$.

Table 3-1 Design Criteria for DC/DC Converter

Tesla Model S (85P) Nominal Battery Voltage 375V	Side-1 Voltage	265V
	Side-2 Voltage	375V
	Side-2 Voltage Range	265~375V
	UC DoD	50%
	Average Inductor Current	160A
	Inductor Current Ripple ΔI	20% @ 160A
	Switching Frequency f	20 kHz

3.2.2 Interleaved Technique

A major challenge for the bi-directional buck-boost converter in HESS application is dealing with high current flowing in and out of the converter [27], [28]. High current reduces the circuit efficiency and produces considerable heat in IGBTs. Assuming that R_{eq} represents the equivalent internal resistance of DC/DC converter, including wiring resistance and inductor resistance, the energy loss is calculated as $P_{DCDC\_loss} = I^2 R_{eq}$. IGBT conduction loss is $P_{IGBT\_on} = V_{IGBTon} I$.

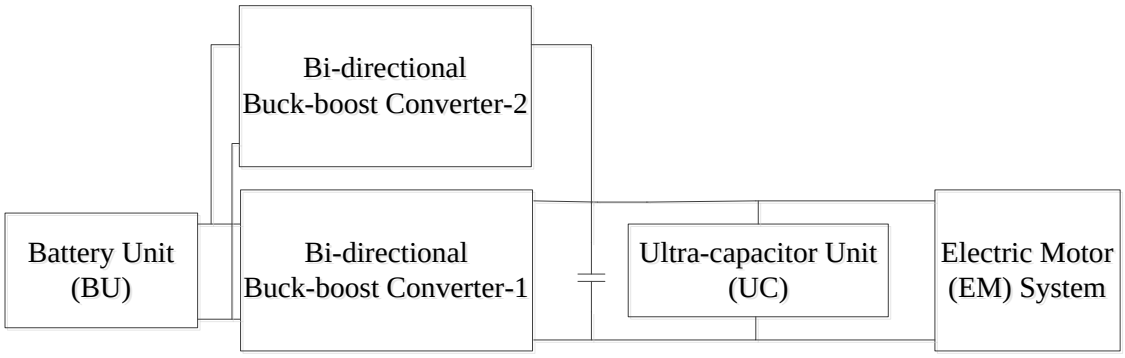

Figure 3-3 Block Diagram of Interleaved Bi-directional Buck-boost Converter

An interleaved boost converter adopts two or more identical DC/DC converters in parallel to share the power and thus current. For instance, if there are two parallel converters, as shown in Figure 3-3, the current value in each one is reduced to half of the value corresponding to one module handling the same total power. Then, $P_{DCDC\_loss} = \left(\frac{1}{2}I\right)^2 R_{eq} \times 2$ and $P_{IGBT\_on} = V_{IGBTon} \times \frac{1}{2}I \times 2$. The power circuit energy loss is reduced by 50%, but switch conduction loss stays the same. Moreover, smaller- current-rating inductors and IGBTs are cheaper and easier to access.

Another important feature that interleaved boost converter offers is current ripple cancelation. High frequency current ripple due to turn-on/turn-off of switches adversely affects battery's life. Possible solutions might be a larger inductor or increased switching frequency, but some side-effects are coupled with these options. The idea of ripple cancelation comes from phase shift between the PWM signals of individual DC/DC converters. The structure of interleaved bi-directional buck-boost converter consisting of two identical DC/DC bi-directional buck-boost converters is shown in Figure 3-4.

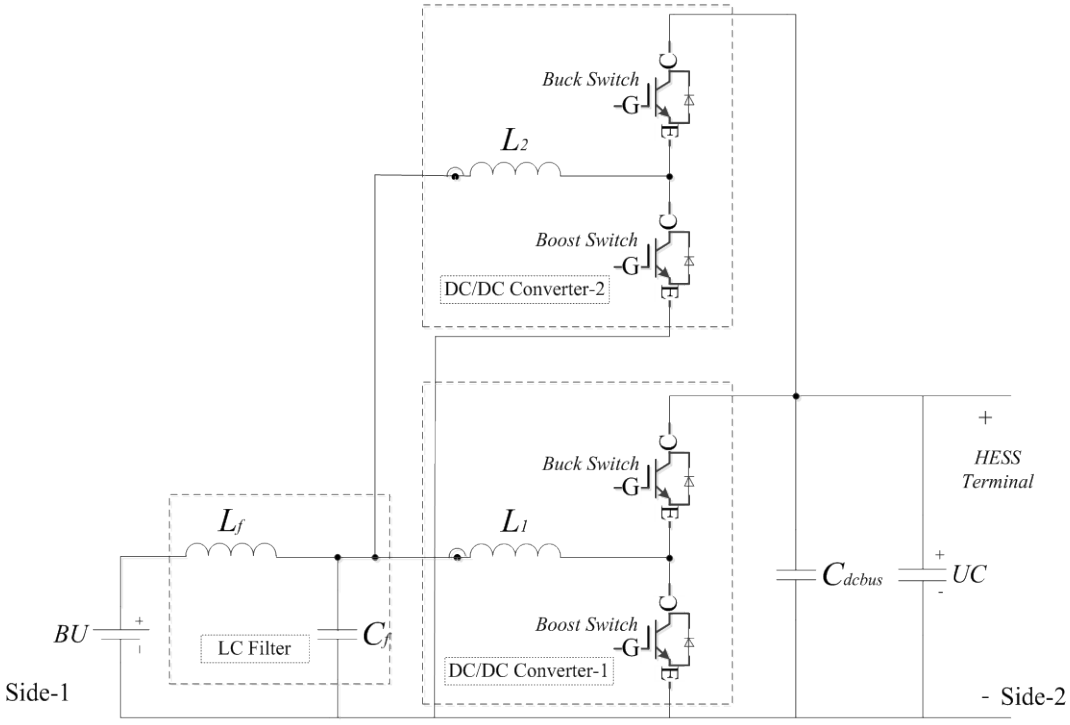

Figure 3-4 Circuit Schematic of Interleaved Bi-directional Buck-boost Converter

Figure 3-5 is the control signals for the switches in the two modules with 180 degrees phase shift between them. In Figure 3-6, the waveform in red represents the current in the first inductor, the waveform in blue is the current in the second inductor, the waveform in pink is the sum of the currents of the two inductors, and the waveform in green is the filtered current of the pink one by an LC filter. The magnitude of current ripple is reduced from 25A to 13A significantly and the ripple frequency is doubled. As a result, a better current quality could be obtained for the battery current using an LC filter.

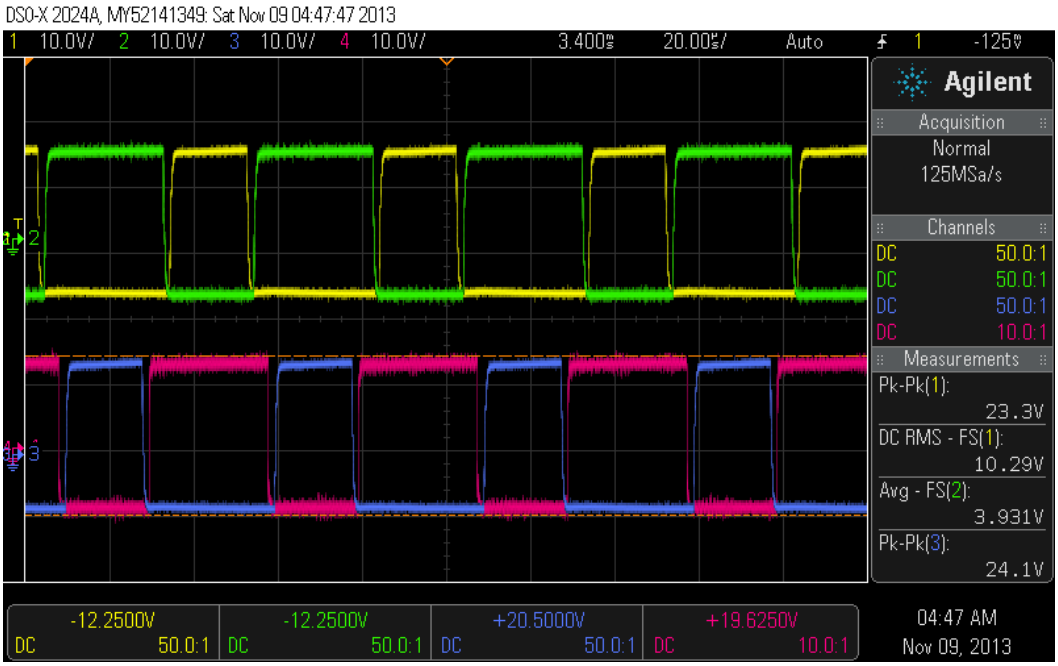

Figure 3-5 PWM Signals for IGBTs of Two Modules: PWM signal for boost switch in module-1 (yellow); PWM signal for buck switch in module-1 (green); PWM signal for boost switch in module-2 (blue); PWM signal for buck switch in module-2 (pink)

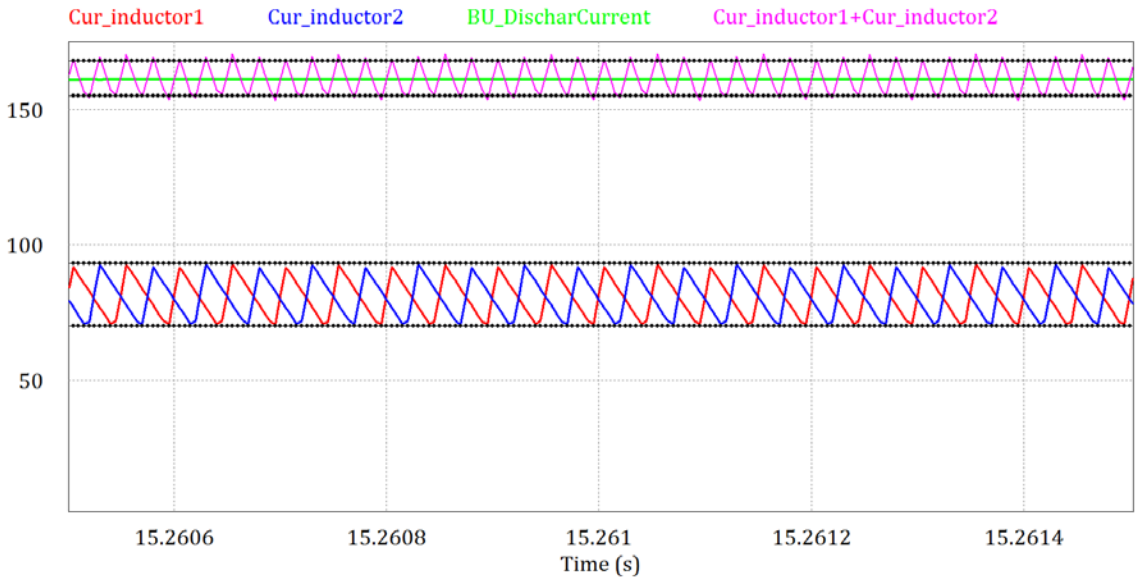

Figure 3-6 Inductor Currents in Individual Inductors and Sum of the Currents of the Two Inductors in the Interleaved Bidirectional Buck-boost Converter and Battery Discharging Current

3.2.3 Soft-switching

IGBTs have limitation in terms of switching frequency. The datasheet of IGBT-cmdus150-12f from Powerex Inc. states that the maximum switching frequency when hard-switched goes up to 30 kHz and maximum switching frequency when soft- switched frequency can reach 70 kHz [29]. Higher switching frequency brings many benefits like smaller current ripple, reduced size of inductor and faster system response. Challenges also come with higher switching frequency, such as increased switching loss, EMI problems, overheating and failure of IGBTs [30]. Soft-switching allows switches operate at higher switching frequencies without creating excessive losses and reduction of reliability. Therefore, soft-switching techniques are very appropriate for HESS.

Soft switching can be performed by implementing resonant circuits or lossless snubber circuits. The circuit composed of resistors, inductors, capacitors and diodes to achieve soft-switching is called snubber. Snubbers can be categorized into two groups based on the use of auxiliary switches, i.e., passive snubber (not including any switch) and active snubber (including switch (es)). Structure of lossless passive snubber is simple. Avoiding a control circuit reduces circuit's complexity. Reference [31] proposed a passive snubber for DC/DC boost converters; but the snubber works with boost converter only and uses nine additional components. Traditional active snubbers have disadvantages of control complexity, hard switching of the auxiliary switches and extra mass due to high current inductor. A novel capacitor-switched snubber for boost converters was introduced with simulation results in [32] and with experiment results in [30]. The bold feature of this novel snubber is non-inductor structure, which simplifies the snubber circuit and its control.

The DC/DC converter in HESS is a bi-directional buck-boost converter. In order to continuously apply the features of capacitor-switched snubber, modification has been made to the original circuit so that capacitor-switched snubber works with bi-directional

buck-boost converter as well. Figure 3.6 shows the capacitor-switched snubber for bi-directional buck-boost converter.

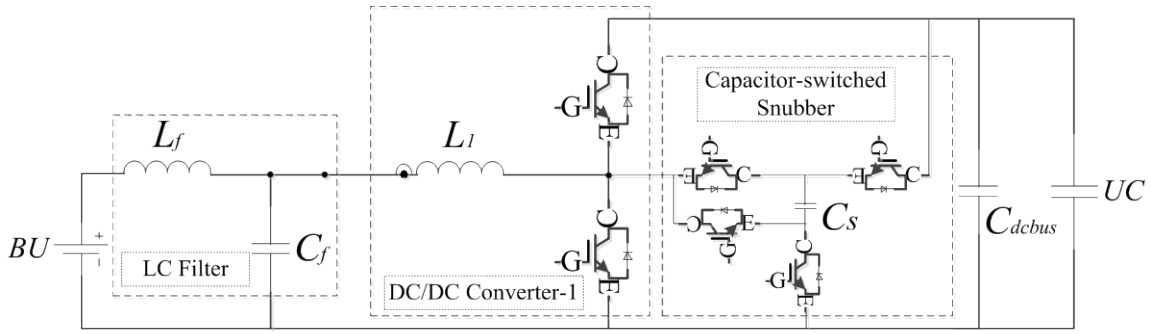

Figure 3-7 Capacitor-switched Snubber for Bi-directional Boost Converter

The major difference between the original capacitor-switched snubber and its modified version is that the diodes used in the former structure are replaced by complete IGBTs coupled with diodes. In boost mode, snubber works in the same way as presented in reference [30]. In buck mode, operation steps of the snubber are explained using Figure 3-8:

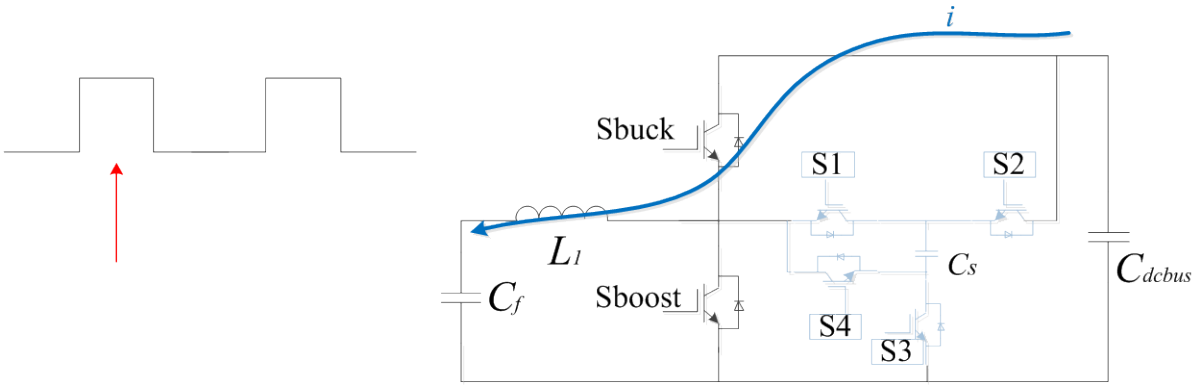

(a)

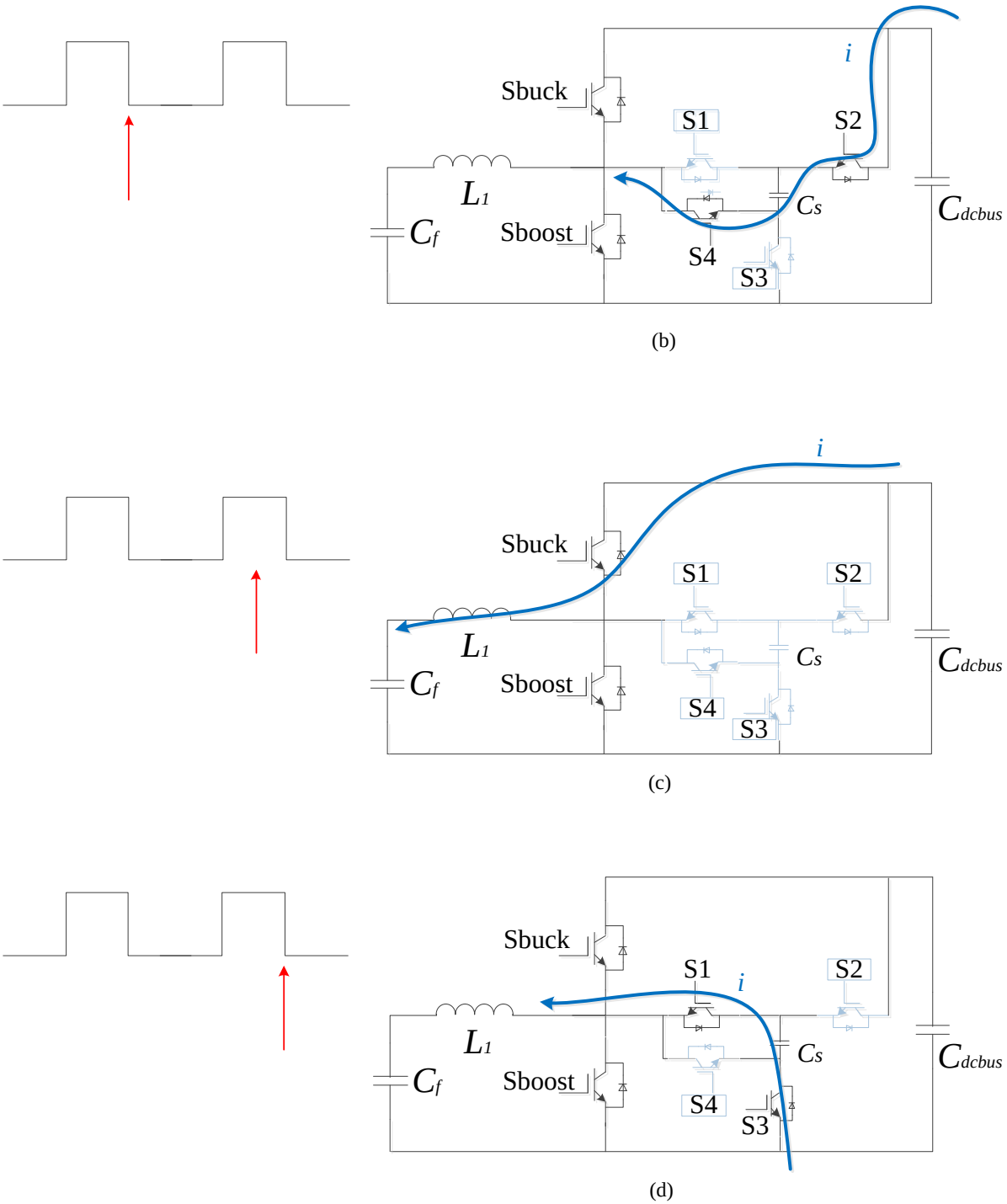

Figure 3-8 Operation of Bidirectional Buck-boost Converter Equipped with Capacitor Switched Snubber When Buck Switch is Turned On and Off

When the bi-directional buck-boost converter is working in buck mode, the power is flowing from high-voltage side (DC bus) towards low-voltage side (battery unit). Assume the switch “Sbuck is initially on, as shown in Fig. 3-8(a). Before the switch “Sbuck” is turned off, switch “S2” is turned on. The voltage across “Sbuck” gradually rises through the path shown in Fig. 3-8(b). This voltage rise is limited by snubber capacitor (C_s) according to $\frac{i}{C_s} = \frac{dv}{dt}$. After this stage, snubber capacitor is charged to a voltage level equal to the DC bus voltage. In the next cycle, “Sbuck” is turned on again, as shown in Figure 3-8(c). Before the second turn-off of “Sbuck”, switch “S1” is turned on. Since snubber capacitor has been charged in the previous cycle, turning on of “S1” will not cause any current surge. When Sbuck is turned off, as shown in Figure 3-8(d), DC bus voltage is equal to snubber capacitor voltage plus the voltage across “Sbuck”. Due to the decrease in the current through “Sbuck”, energy is withdrew from snubber capacitor in order to keep inductor current continuous. Based on $\frac{i}{C_s} = \frac{dv}{dt}$, gradual drop in snubber capacitor voltage leads to gradual rise in voltage across “Sbuck”. Steps (a) and (b) will be repeated in the next cycle. Each time “Sbuck” is turned off, capacitor-switched snubber delays the voltage rise across “Sbuck”.

Simulation results obtained from Pspice simulation package are given in Figure 3-9. The green waveform represents the current through “Sboost” in boost mode and “Sbuck” in buck mode, the red waveform represents the voltage across “Sboost” in boost mode and “Sbuck” in buck mode, and the blue waveform represents current flowing in snubber capacitor. The waveforms of the voltages across the switches “Sboost” and “Sbuck” clearly show the reduction in the rate of rise voltage at turn-off due to using the capacitor-witches snubber circuit, as well as charging and discharging of the snubber capacitor in successive turn-off events.

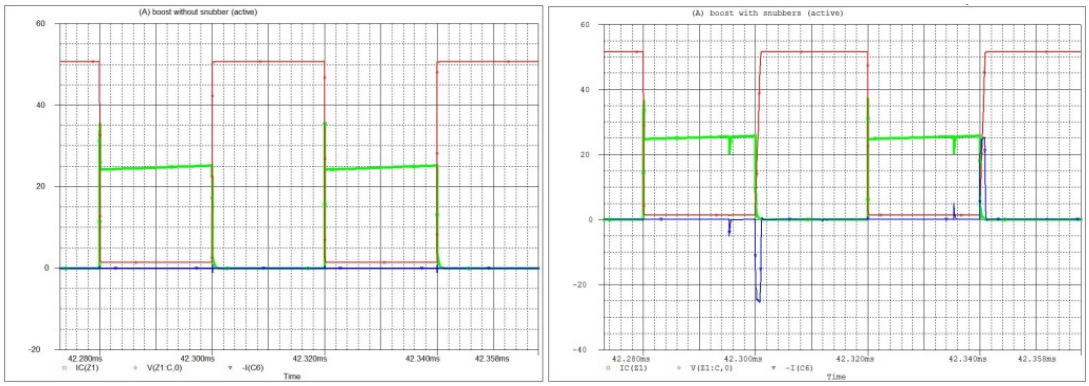

(a) boost mode without snubber (b) boost mode with snubber

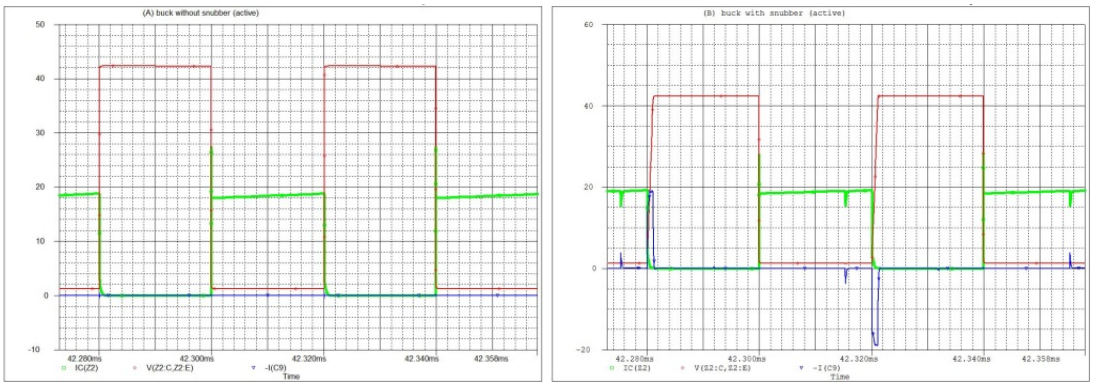

(c) buck mode without snubber (d) buck mode with snubber

Figure 3-9 Simulation Results for Soft-switching

3.3 Design of HESS power management

Cooperation of battery and ultra-capacitor is dictated by the HESS power management algorithm with respect to their respective characteristics. The selected HESS configuration has the BU under full control by a DC/DC converter. The power management aspects on BU include:

- *Maximum battery discharge current*: Experimental results in reference [33] revealed the capacity fades of 9.5%, 13.2%, and 16.9% for Sony US 18650 lithium-ion battery cell after 300 cycles at three different discharge current rates

of 1C, 2C and 3C. By definition, 1C corresponds to the current level that can charge battery cell from empty to full in one hour or discharge battery cell from full to empty in one hour. The results clearly showed that higher discharge current rate accelerates battery's degradation.

- *Maximum rate of rise of battery charge/discharge power*: This index refers to slope of battery power change $\frac{dP}{dt}$. Equivalently, it also means maximum rate of rise of battery charge/discharge current due to battery terminal voltage's small variation. This condition protects battery power from fast-changing charge/discharge current.
- *Maximum battery charging current and maximum battery charging voltage*: In terms of battery charging, there are two possible scenarios. In the first scenario, BU in the vehicle is charged by the grid following the most commonly used charging method, which is constant-current constant-voltage (CC-CV) scheme [18], [33]. The second scenario refers to energy recycling where battery is charged by the regenerative braking energy.
- *DC bus voltage regulation*: The physical connection of DC bus with electric motor drive requires the voltage variations on the DC bus to be within EM's input voltage range. Both overvoltage and under-voltage can cause malfunction of EM system. Hence, BU is controlled to charge UC or absorb energy from UC when necessary to keep the DC bus voltage within specified safe limits.

Based on the conditions described above, the specific power management algorithm for the designed HESS in simulation is summarized as follows:

- BU maximum discharge current is limited to 0.5C. Tesla Model S has a battery pack rated at 85 kWh, with around 8000 battery cells. In order to satisfy side-1 voltage requirement in the HESS, the battery pack terminal voltage should be reduced to 265V by re-configuration of the cells in series and in parallel. Battery

pack capacity then becomes 320Ah. In simulation, $\max I_{BU-discharge}$ becomes equal to 160A.

- $\frac{dP}{dt} = 8kW/s \Leftrightarrow \frac{di}{dt} = 30.2A/s$
- BU maximum standard charging current is 0.5C and standard charging voltage is 4.2V per cell, according to the datasheets. Charging conditions in simulation are: $\max I_{BU-charging} = 160A$ and $\max V_{BU-charging} = 309V$.
- Input voltage range of electric motor system is unknown. DC bus voltage regulation is assumed to be in the range 325V~375V. UC will be charged by BU if DC bus voltage drops to below 325V, and BU will be charged by UC if DC bus voltage exceeds 375.

3.4 Design of Controller for DC/DC converter

Fundamentally, a negative feedback control system will be required to make the controlled variable follow closely the reference. In the dynamic model of buck converter, output voltage $v_{out}(t)$ become the function of input voltage $v_{in}(t)$, duty cycle $d(t)$, and output current $i_{out}(t)$ [34]. In case of boost converter with controlled current, input current $i_{in}(t)$ is the function of input voltage$v_{in}(t)$, output voltage $v_{out}(t)$, and duty cycle $d(t)$. Figure 3-10 shows the closed-loop control system for regulation of the input current (i.e., BU current in HESS).

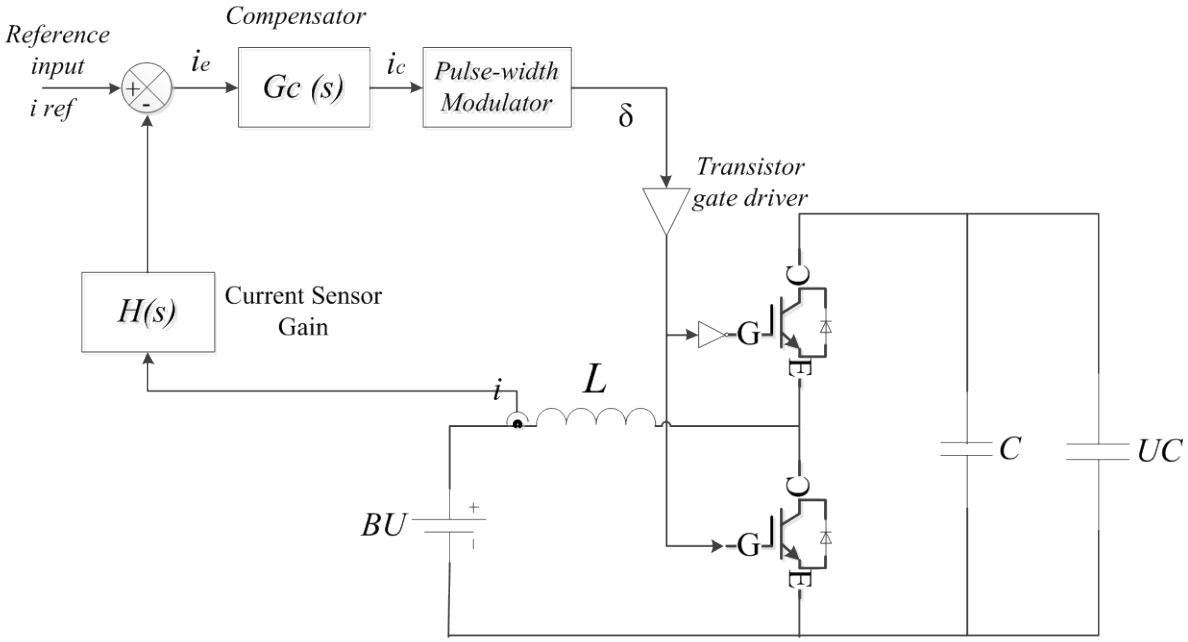

Figure 3-10 Negative Feedback Loop for Input Current Control in Bi-directional Buck-boost Converter

Inductor current is measured by a current sensor with gain $H(s)$. The difference between current reference and current sensor output is the current error. Ideally, there is no error at steady state, $i_{ref}(s) = H(s)i(s)$. The output of the controller controls switch duty cycle in order to pull the error back to "0" whenever the current deviates from its reference. Circuit response to reference changes is determined by the compensator block in the feedback loop. Small value of $G_c(s)$ makes the circuit to adjust slowly to the reference. On the other hand, large value of $G_c(s)$ makes the circuit sensitive to reference. The procedure to find an appropriate set of $G_c(s)$ value is called "tuning". Generally, a PD, a PI or a PID compensator is used for controller, Among these, PID compensator offers advantages of both PD and PI controllers, which are large bandwidth and zero stead-state error [34].

Since PI compensator is a simple and effective approach, the controller designed for HESS is based on it. The block diagram of the PI controller for the DC/DC converter in HESS is shown in Figure 3-11.

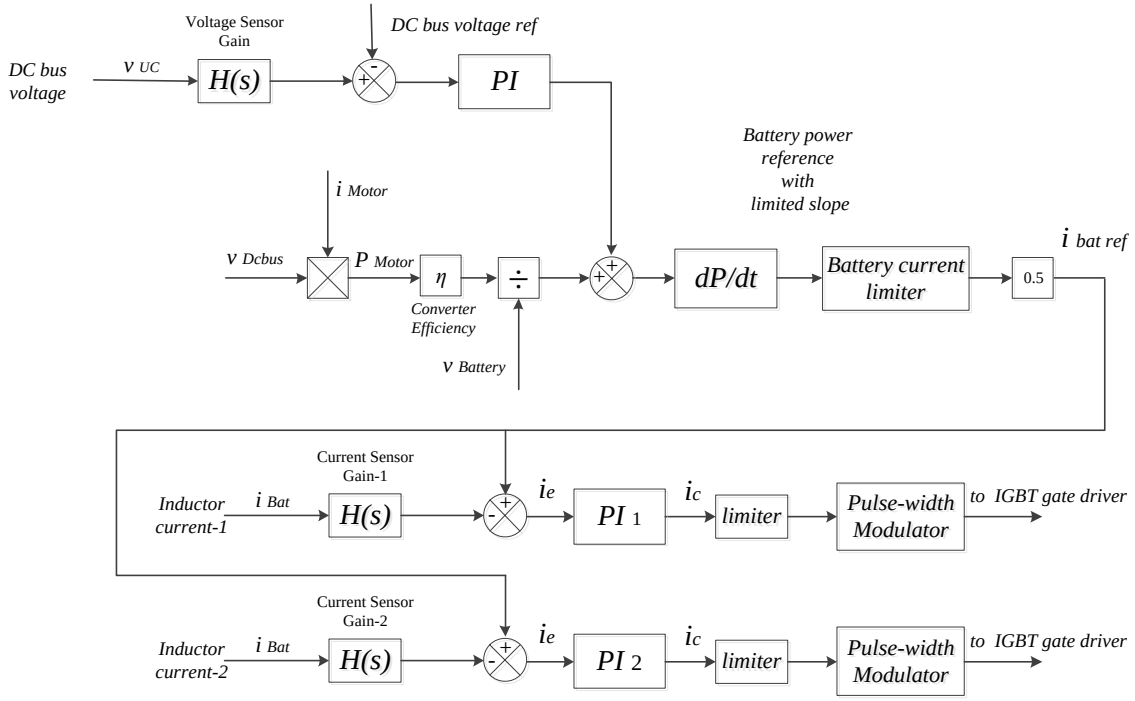

Figure 3-11 Block Diagram of PI-based Controller for HESS DC/DC Converter

3.5 HESS Integration with Battery Charger

PEVs and PHEVs are primarily used during day time, and their batteries are recharged to full storage capacity either by a single/three phase charging station or overnight by easily plugging in the single phase grid at home. Both scenarios require an on-board battery charger matched with the battery pack. Among different structures of level-2 on-board battery chargers, the two-stage cascade topology, shown in Figure 3-12, is fully documented in the literature [18], [35]. The cascade structure is consisting of an AC/DC converter and a DC/DC converter. The AC/DC converter is responsible for input current

wave-shaping, power factor correction and dc link voltage regulation, while the DC/DC converter is for battery charging current control.

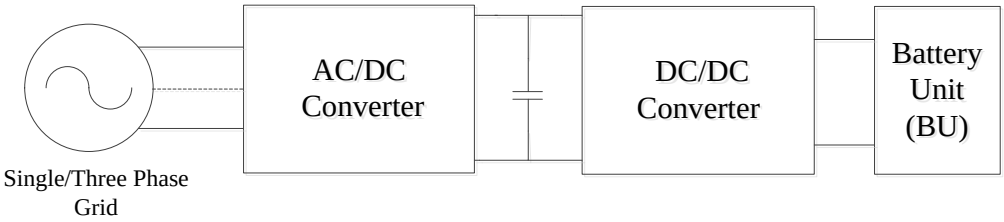

Figure 3-12 Two Stage On-board Battery Charger Topology

There are four possible options for the connection of the on-board battery charger with HESS. Figure 3-13 presents the most straightforward scheme featuring direct connection of the battery charger to the BU. UC can be also charged if the bi-directional DC/DC converter of HESS operates at the same time.

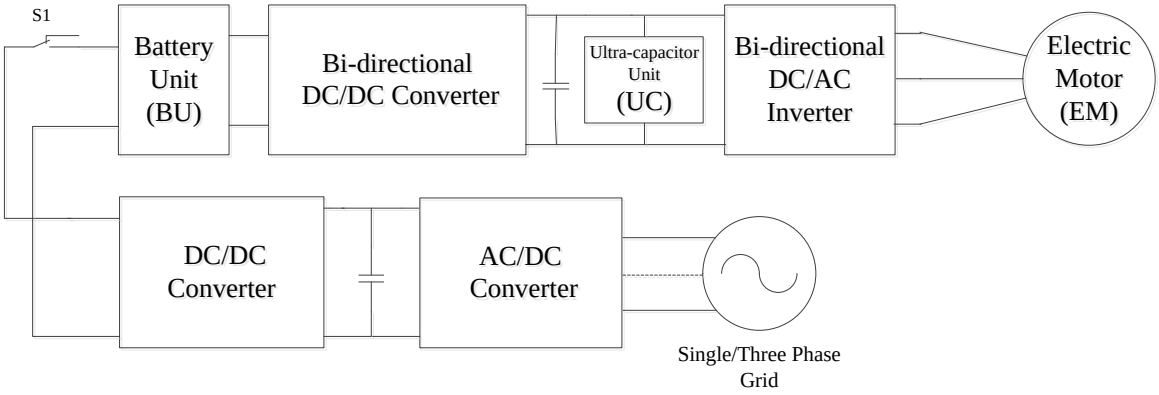

Figure 3-13 Integration of HESS with Battery Charger – Scheme 1

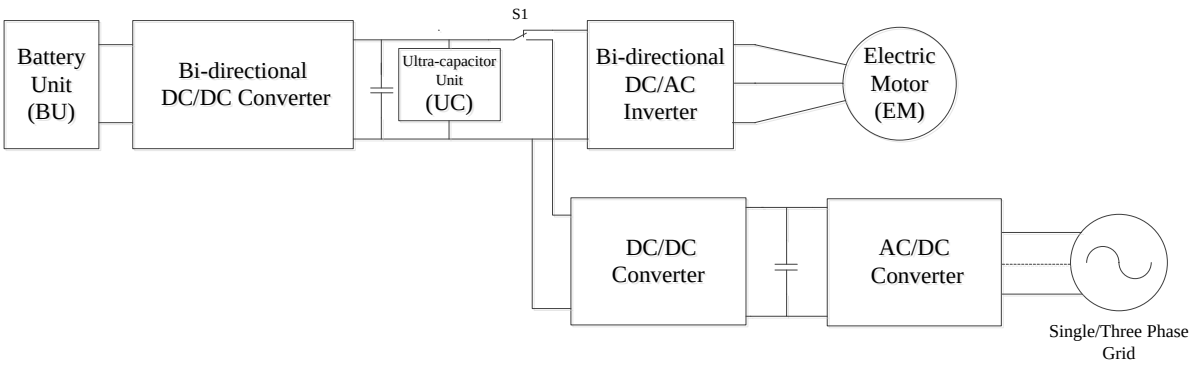

Figure 3-14 Integration of HESS with Battery Charger – Scheme 2

The second scheme for integration of HESS with battery is shown in Figure 3-14. The single-pole, double throw switch "S1" will be used to disconnect the traction motor inverter when the vehicle is ready for charging. UC will be charged first to its nominal voltage before the charging of the battery begins. In this scheme, the presence of the bi-directional DC/DC converter of HESS and the DC/DC converter of battery charger reduces the energy transfer efficiency from the grid to the on-board BU. Therefore, the DC/DC converter stage is removed in the third scheme presented in Figure 3-15.

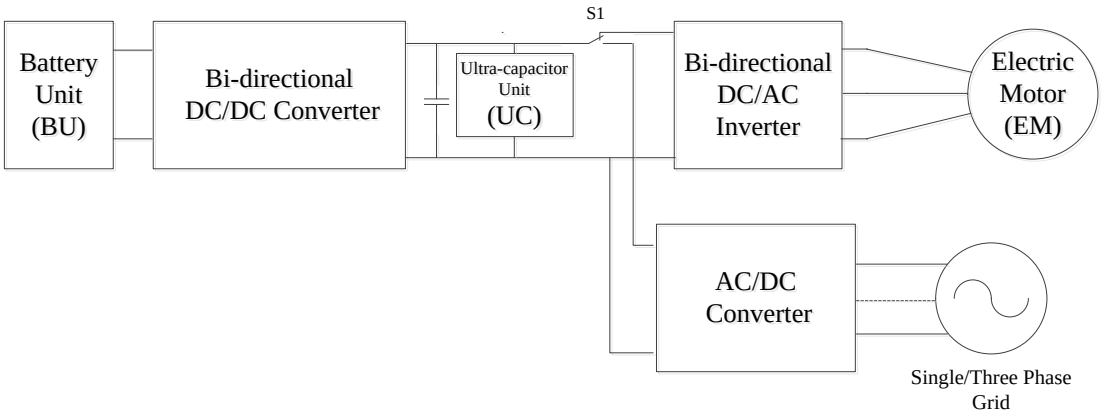

Figure 3-15 Integration of HESS with Battery Charger – Scheme 3

Previous work [36] has considered the bi-directional DC/AC motor drive inverter for interfacing the battery to the grid. Thus, more cost will be saved by sharing the bi-directional DC/AC inverter between HESS and battery charger, as shown in Figure 3-16.

The presence of UC on the DC bus brings the additional benefit of stabilizing the DC bus voltage during charging. When a PEV or PHEV is stationary and ready to be charged, the switches “S1”, “S2”, and “S3” assume the position for battery-charging mode. When the vehicle is ready to be driven, the switches “S1”, “S2”, and “S3” are used to disconnect the vehicle from the grid and enable HESS mode.

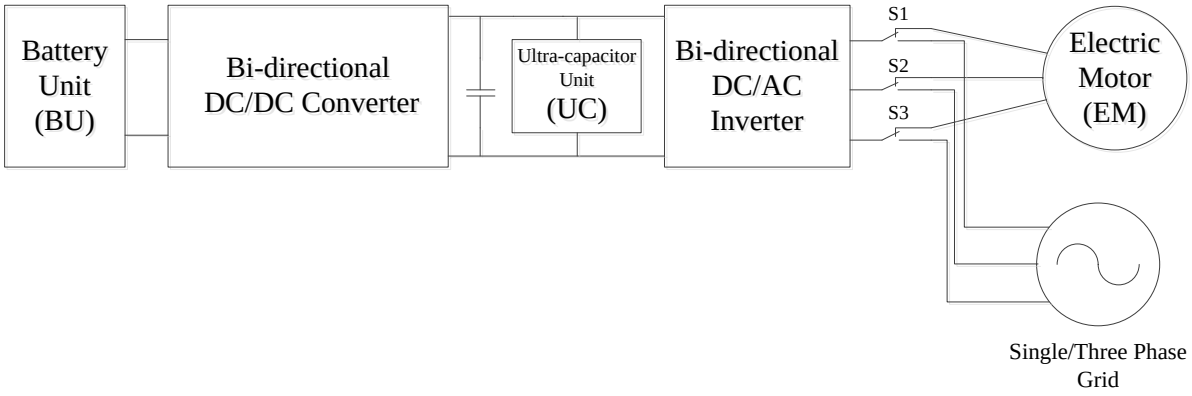

Figure 3-16 Integration of HESS Charger in the Electric Powertrain – Scheme 4

3.6 HESS Simulation – Case Study

The technical aspects of HESS were reviewed and analyzed in the previous sections. Finalized HESS schematic is shown in Figure 3-17. The system can be divided into 5 parts, i.e., battery unit (BU), LC filter, DC/DC converter, ultra-capacitor unit (UC) and an emulated electric motor (EM) system. Simulation is conducted using PSIM simulation package. In contrast with PSPICE, PSIM is not based on the actual models of the components used in implementation. As a result, efficiency issues cannot be realistically considered. BU model in PSIM (Figure 3-18) is derived based on the battery model discussed in Chapter 2. A simulation-friendly model for UC is shown in Figure 3-19.

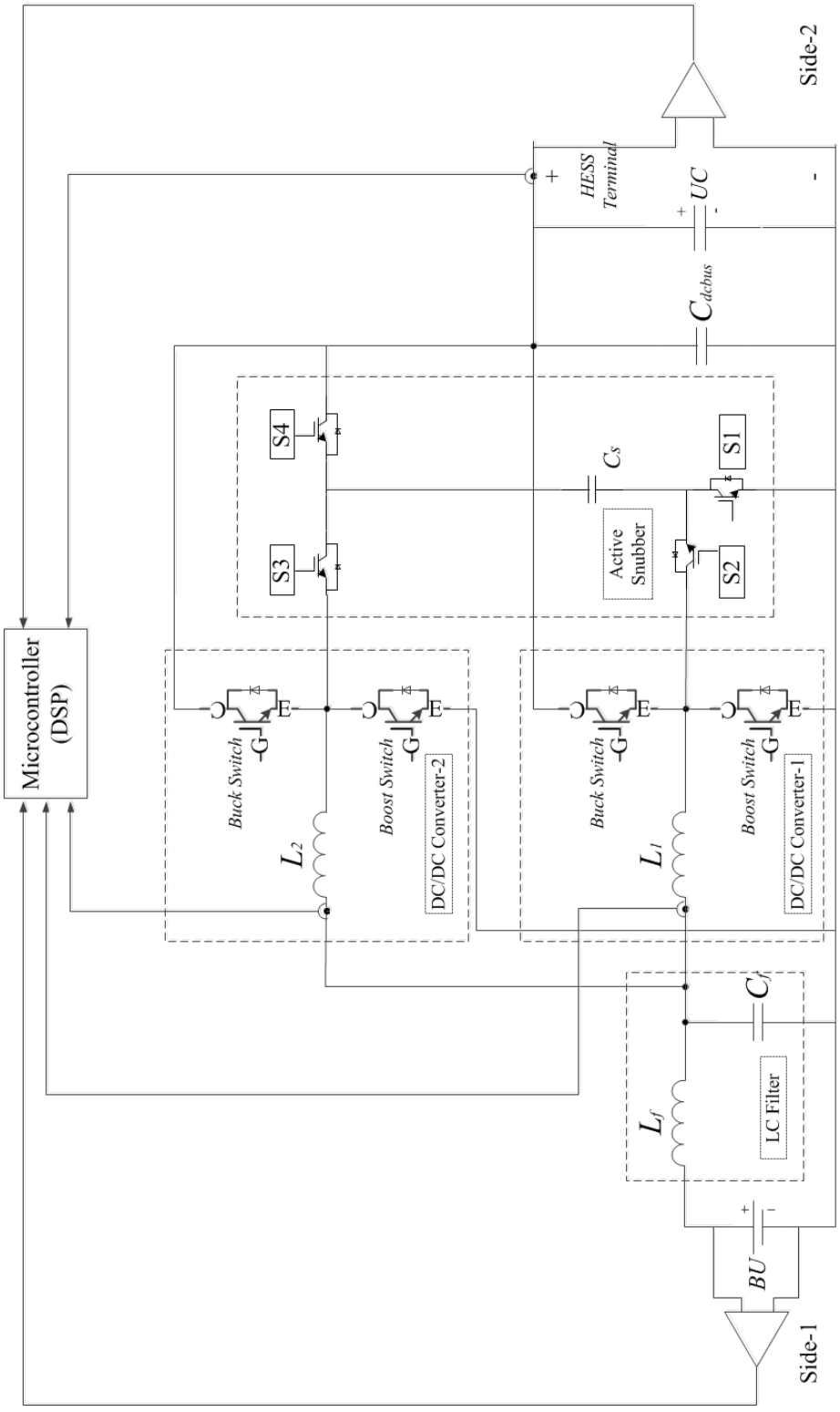

Figure 3-17 Finalized HESS Circuit Schematic

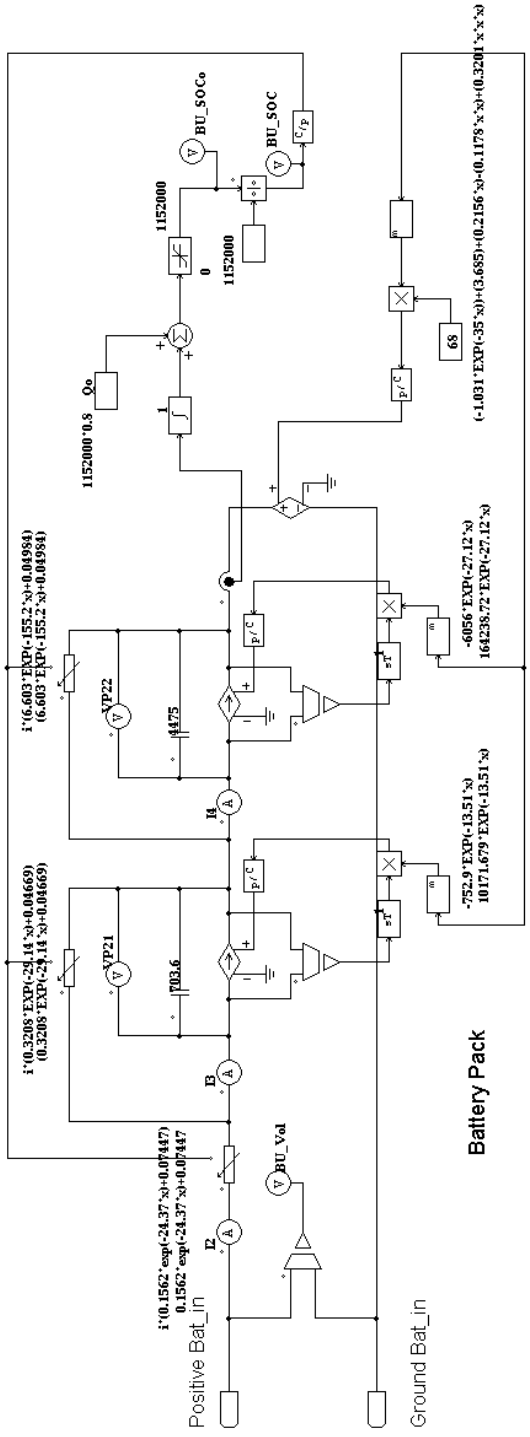

Figure 3-18 Battery Model in PSIM

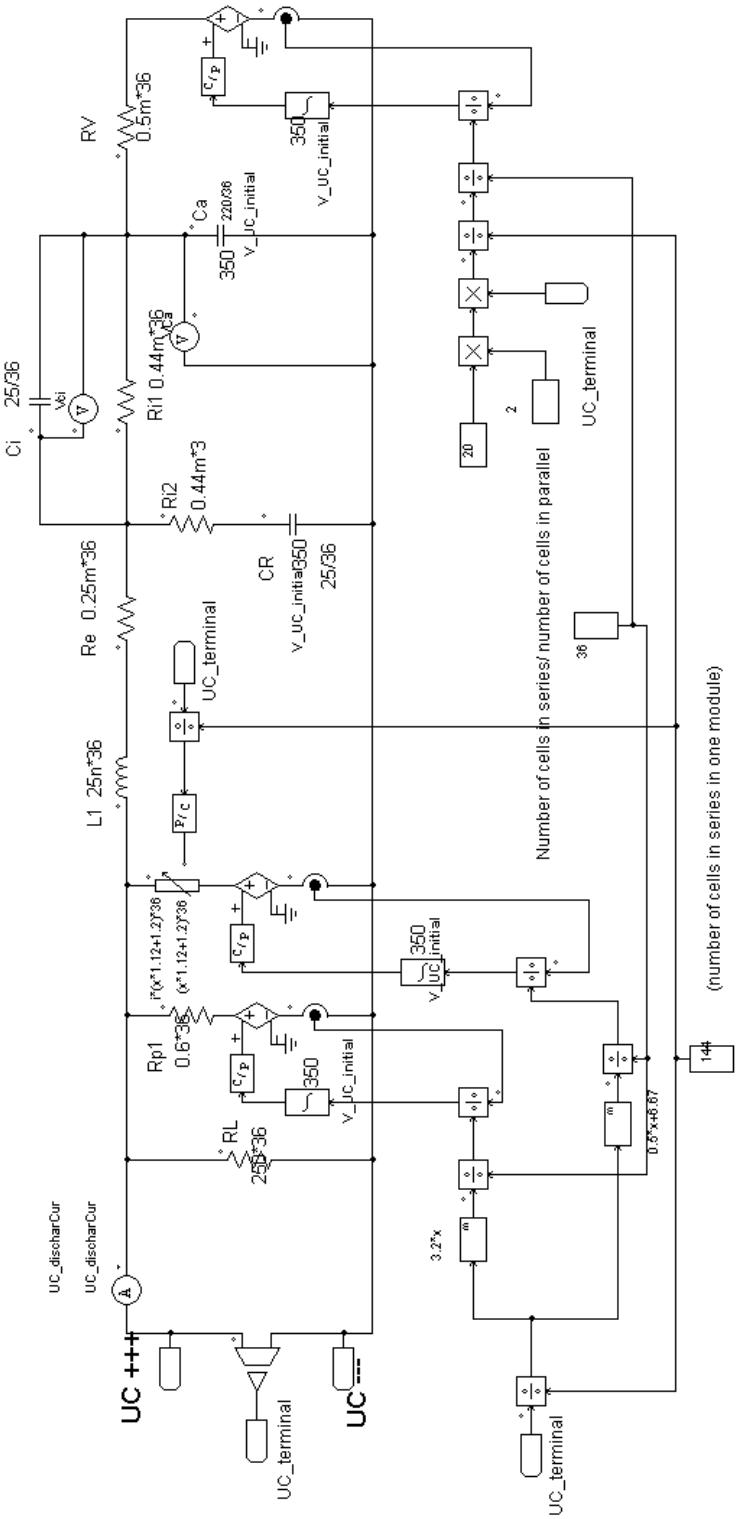

Figure 3-19 UC Model in PSIM

The LC filter on the battery side plays an important role to smooth battery charge/discharge current. Design of LC filter is based on cutoff frequency and damping ratio.

$$\omega_c = 2\pi f_c = \frac{1}{\sqrt{LC}} \tag{3.4}$$

$$\xi = \frac{R_L + R_c}{2}\sqrt{\frac{C}{L}} \tag{3.5}$$

where R_L and R_C are the equivalent series resistances of filter inductor and capacitor. The current ripple frequency in each inductor is 20 kHz, i.e., the same as the switching frequency. Because of interleaved structure, magnitude of current ripple is reduced and current ripple frequency is doubled to 40 kHz. Cutoff frequency of the LC filter is typical selected as one tenth of the ripple frequency. Therefore,

$$f_c = \frac{1}{2\pi\sqrt{LC}} = 4k \tag{3.6}$$

A typical value for damping ratio is 0.7. Thus,

$$\frac{R_L + R_c}{2}\sqrt{\frac{C}{L}} = 0.7 \tag{3.7}$$

Utilizing a complete model of inverter and EM as the load for HESS is doable in PSIM simulation, but using a combination of two voltage-controlled current sources to emulate bidirectional power exchange between HESS and EM gives more flexibility and control to the study. In Chapter 2, the power profile of Tesla Model S (85P) on UDDS drive cycle was derived based on a series of equations. Therefore, to avoid unnecessary calculations, the data representing consumed power by Tesla on a certain drive cycle, is imported for simulation purposes (see Figure 3-20). Simulation results are given in Figure 3-21.

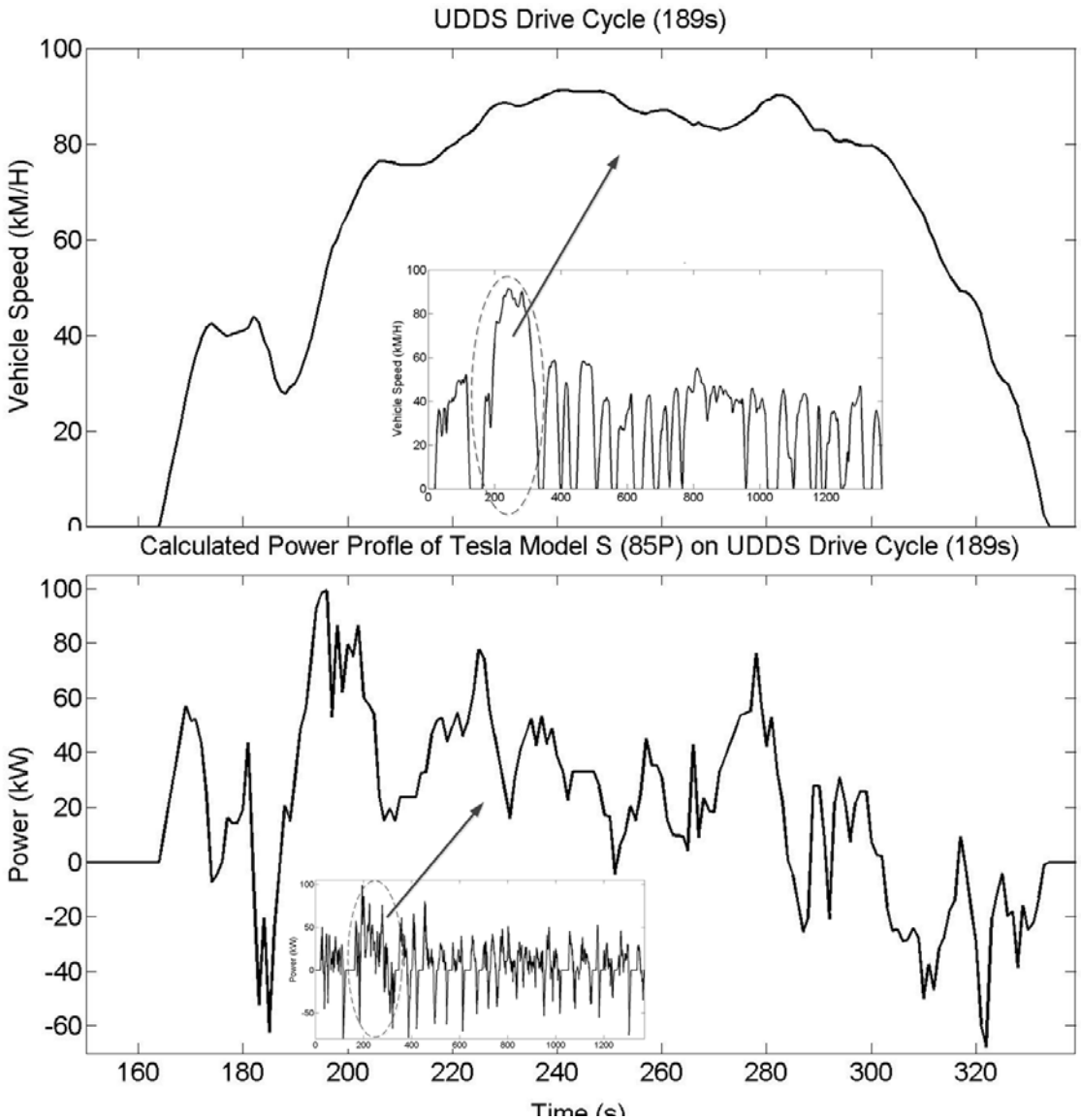

Figure 3-20 189s of UDDS drive cycle and the corresponding power profile for Tesla Model S

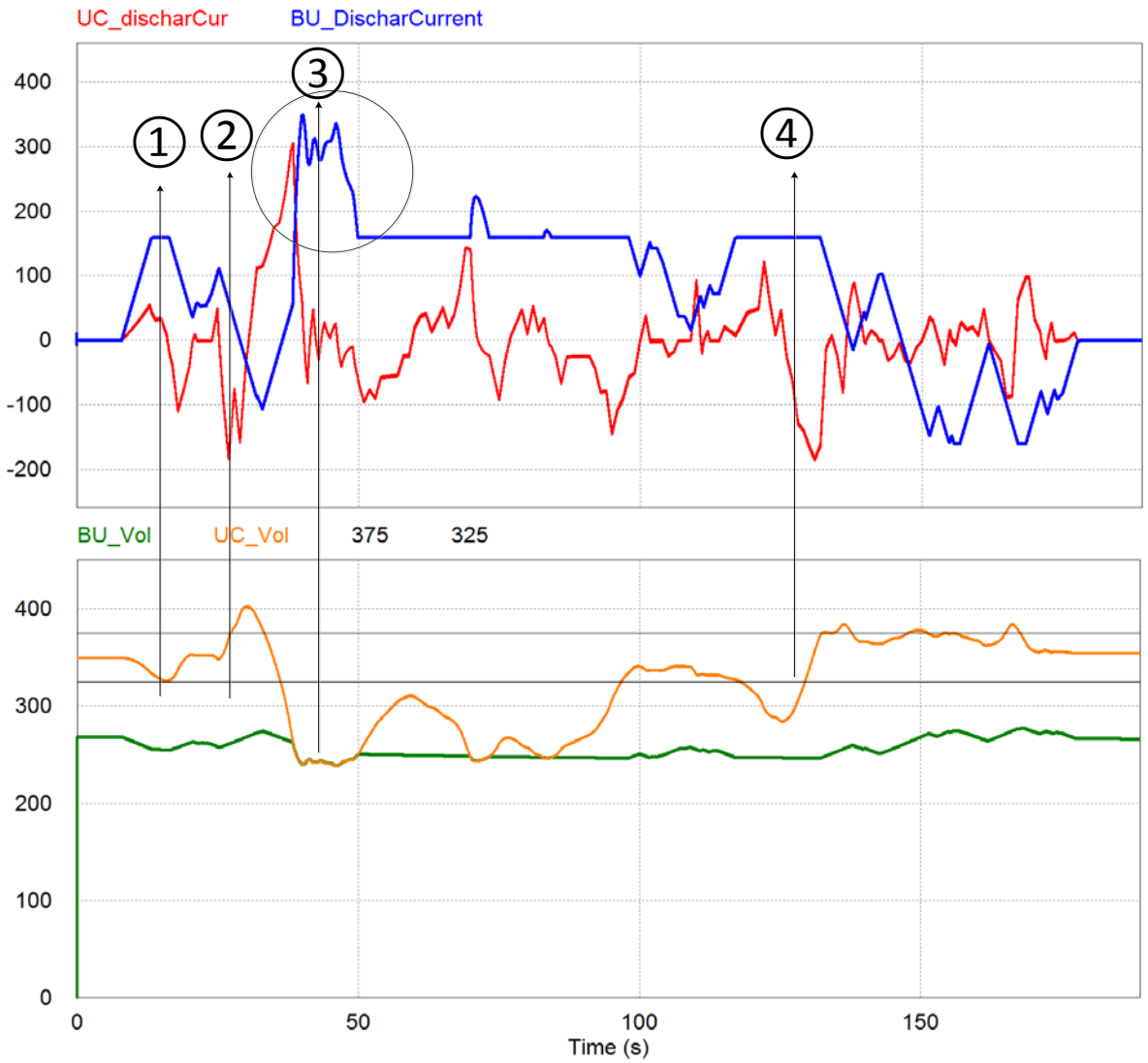

Figure 3-21 BU discharging current, UC discharging current, BU terminal voltage, and UC terminal voltage from PISM simulation for Tesla Model S on the 189s of the UDDS drive cycle

The time for Full UDDS drive cycle is 1,389 seconds. The data representing vehicle power used in PISM simulation covers just 189 seconds. The top waveform in Figure 3-20 shows the drive cycle used in simulation and the bottom waveform in Figure 3-20 represents the corresponding power profile for Tesla Model S on the 189s of UDDS drive cycle. The blue waveform in Figure 3-21 is battery discharging current and the red waveform is ultra-capacitor discharging current. The green waveform is battery pack

terminal voltage and the orange waveform is ultra-capacitor pack terminal voltage. The numbers marked in Figure 3-21 stand for different scenarios of HESS operation. In the first point (1), the vehicle is accelerating. BU and UC together provide power to the vehicle. It is noted that battery discharging current is limited to 160A. The second point (2) shows that UC voltage increases to the upper limit (375V) as a result of collecting the regenerative braking energy. The extra amount of energy flows back to BU under the control of DC/DC converter. In point three (3), it is noted that battery discharging current exceeds the upper limit. This is a special case in which vehicle needs a high level of power to achieve an aggressive acceleration. UC voltage has dropped to its minimum that equals the BU voltage. DC/DC converter is no longer working in boost mode. Instead, BU is discharging through the boost diode. When the vehicle speed goes up, battery power drops back to within its nominal range. Generally, aggressive acceleration will not last very long and battery is capable of short-time high-current discharging. The last point (4) indicates that BU provides power to EM and charges UC, as well, since UC voltage is lower than its minimum allowable value.

It is noticed that in scenario three (3), the high battery discharge current will go through the boost inductors in the DC/DC converter. If the design of the boost inductors considers the maximum current surge, very large boost inductors will be chosen for high current capability of 190A (assuming the DC/DC converter is interleaved), which is very uneconomic. In the case of Tesla Model S on the full UDDS drive cycle, scenario three (3) occurs in only 6% (83 seconds over 1370 second) of the total period. In reference [14], a bypass power diode is connecting BU to UC to provide a current pass for current surge like in scenario three (3). This method will bring extra conduction loss when the bypass power diode is conducting current. Figure 3-22 shows an alternative method with a high current relay. Relay is some kind of mechanical switch with almost no conduction loss. It has relatively slow response at turn on and turn off (in miliseconds), but it works for this case, since a fast response is not required. Figure 3-23 shows the simulation results for current through the inductors and the relay. Waveform in blue in the top

diagram is the battery discharge current; waveform in red in the top diagram is the current through the relay contact.

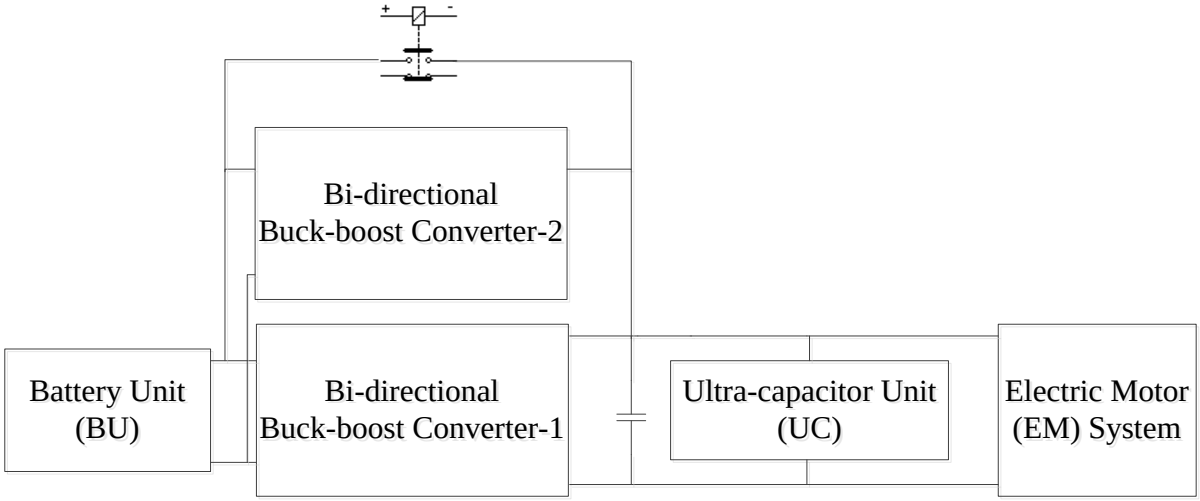

Figure 3-22 HESS with a Bypass Relay

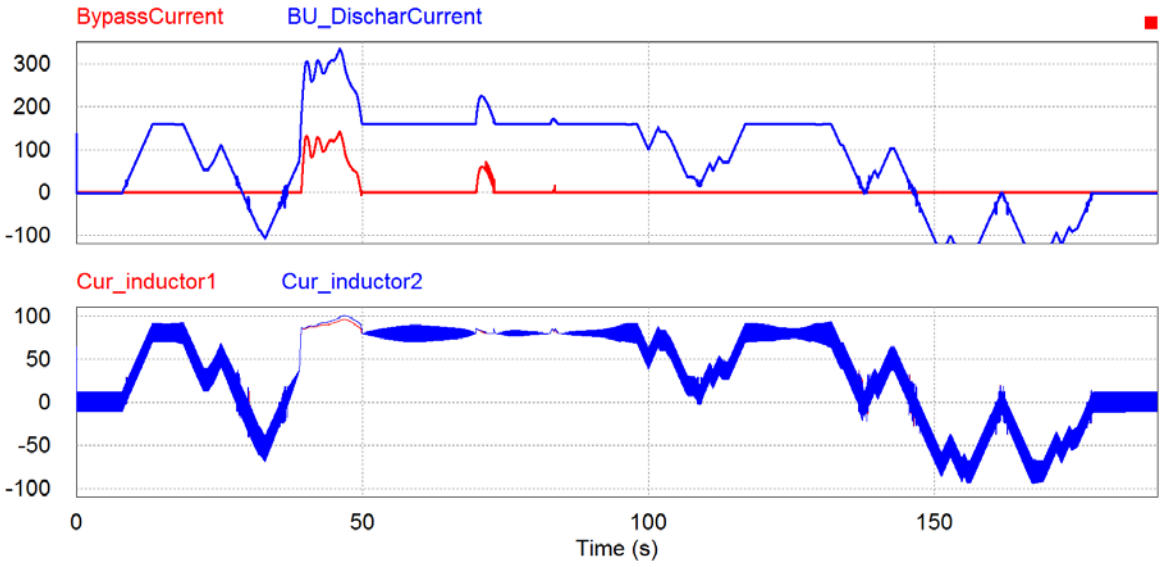

Figure 3-23 Simulation Results of HESS with the Bypass Relay

3.7 Summary

Partially-decoupled HESS topology, with UC directly connected to DC bus, is selected for study in this thesis due to its relatively-low cost and small size. A bi-directional buck-boost converter interfaces BU and UC to control battery discharge/charge behavior. The BU is on the low-voltage side (to reduce cell balancing cost) and UC is on the high-voltage side. Interleaved structure with two parallel DC/DC converters helps cancel the high-frequency current ripples so that smaller inductors need to be used. The two DC/DC converters will share the total power, which results in improvements in the converter's efficiency. Soft-switching are crucial in reduce IGBT's switching losses to make it possible to operate switches at higher frequencies while maintaining high energy efficiency.

HESS power management takes into consideration maximum battery discharge current, maximum rate of rise of battery charge/discharge power, lithium-ion battery's charging behavior in CC and CV modes, and DC bus voltage regulation. The power management algorithm is realized by a PI based negative feedback control system. For a special case in which high current surge occurs, a bypass relay interfacing BU and UC provides a path for current surge to keep the inductor current within the designed limit.

Due to the similarities in the structure between the selected HESS and a documented on-board battery charger, the integration of HESS with battery charger can save one AC/DC converter and one DC/DC converter.

Chapter 4

HESS Prototype Development

4.1 Preliminary HESS Design Criteria

In addition to the HESS design procedures discussed in Chapter 3, HESS prototype development should respect hardware limitations in the laboratory as well. Table 4-1 records the available hardware resources for HESS prototype development and HESS performance testing. Details of these components can be found in Appendix B.

Table 4-1 Available hardware resources for HESS prototype

Item	Description
Battery Pack	GBS lithium-ion battery with 25.6V and 40Ah at 100% SoC
Ultra-capacitor Module	Maxwell ultra-capacitor module rating at 16V/58F
IGBT Module	600V voltage limit and 150A current limit
DSP	TMS320F2808 DSP Experimental Kit
Sensors	Current transducer for -100A to 100A; Voltage transducer for 10V to 500V
Inductors	High-frequency DC inductors: 360uH, 500uH, 1.3mH
Capacitors	1mF and 2.4mF high-current-ripple electrolytic capacitors
DC Power Source	Xantrex DC power source 9A-300V
DC Power Load	Chroma electronic load 63804, 350V/45A/4.5kW

Functionality of HESS prototype is going to be verified using a test setup. The most effective test setup for this purpose is an AC traction motor system connected with a controllable-torque load to fully emulate road condition. However, due to the complexity of such a system, and the long time required for its development, alternative approaches for testing HESS are going to be considered in this thesis. The first option (Option 1) is a DC motor-based test bench, as shown in Figure 4-1. The DC motor is operated under speed control to follow a particular drive cycle while the flywheel provides a load torque to the DC motor shaft proportional to the change in its rotational speed. Since HESS DC bus is connected to the motor controller, DC bus voltage has to meet the input requirement of the DC motor controller, which has a range of 24V to 48V.

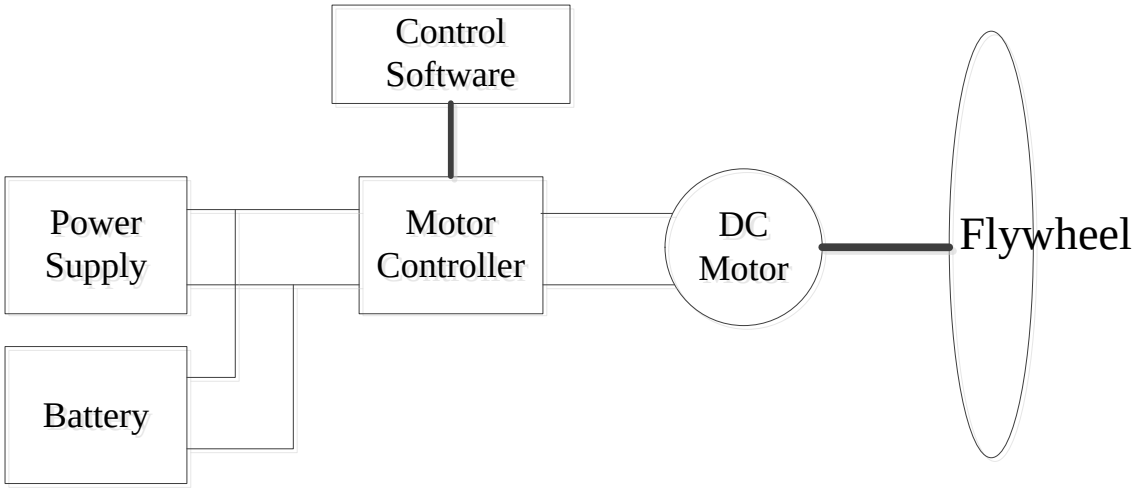

Figure 4-1 Block Diagram of HESS with DC Motor-based Test Bench

Another possible test setup (Option 2) is a small-size electric vehicle, “ZENN 2008”, whose traction motor is an AC asynchronous motor with a 48V-to-80V DC input voltage range. Table 4-2 lists system specifications of the above two options.

Table 4-2 Specifications of two test setup options for HESS

	Option 1	Option 2
Motor	DC motor (D&D)	AC motor (Advanced Motor & Drivers)
Rated Power of Motor	4.6kW	5.69kW
Controller	NAVTAS TSX	Curtis 1236-63XX
Input Voltage Range (DC)	24-48V	48V-80V
Nominal Motor Current	191.7A	118.5A
Peak Motor Current	200A	181.3A

In order to simplify the problem and make it possible for the tests to be performed in a regular power electronics lab, before moving to a motor-based test setup, the vehicle load as seen by HESS prototype is realized by combining a programmable load and a DC source. This “controllable power load” is shown in Figure 4-2(a). Power profile of a DC motor-based test setup (see Figure 4-2(b)) is recorded via the dSPACE control panel. Data is then imported to the controllable power load to realize the same power profile.

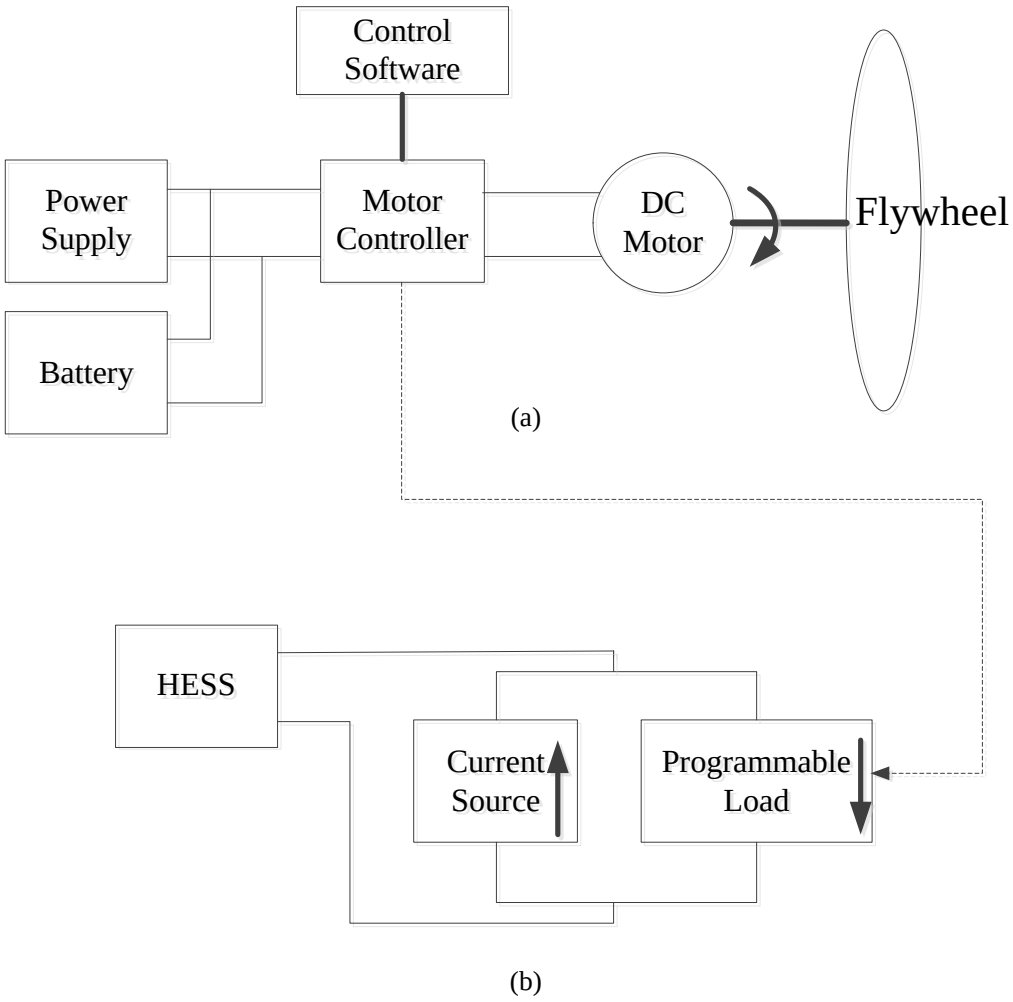

Figure 4-2 (a) DC Motor-based Test Setup; (b) HESS with Controllable Power Load

The main advantage of the controllable power load is the capability and flexibility of emulating any vehicle behavior on any drive cycle, since power profile can be calculated from the equations listed in Chapter 2 or extracted from a motor-based test setup. Another benefit that controllable power load brings is guaranteed safe operation of the system by setting the limits for voltage, current and power, preventing HESS prototype from being damaged due to malfunctioning during debugging stage of HESS prototype.

The programmable power load, “Chroma 63804”, is capable of drawing currents up to 45A and powers up to 4.5kW. It is remotely controlled to operate in constant-power (CP) mode by a software panel. The current source is the “Xantrex 9-300” DC source with maximum current of 9A and maximum voltage of 300V, operated in constant-current (CC) mode. Combination of programmable power load and current source provides HESS with positive power, negative power or zero power. Positive power means that power value of programmable power load is larger than that of DC source, emulating vehicle’s acceleration. On the contrary, negative power implies that power value of programmable power load is smaller than that of DC source, emulating vehicle’s deceleration during regenerative braking.

4.2 HESS Prototype

A HESS prototype with scaled-down power level was developed in the laboratory as a proof of principle. Figure 4-3 shows different components of the HESS prototype. Figure 4-4 presents a photograph of the completed HESS prototype, Table 4-3 lists parameters of the designed HESS prototype and Figure 4-5 is the flow diagram of HESS power management. Coding of the control algorithm in C language can be found in Appendix C.

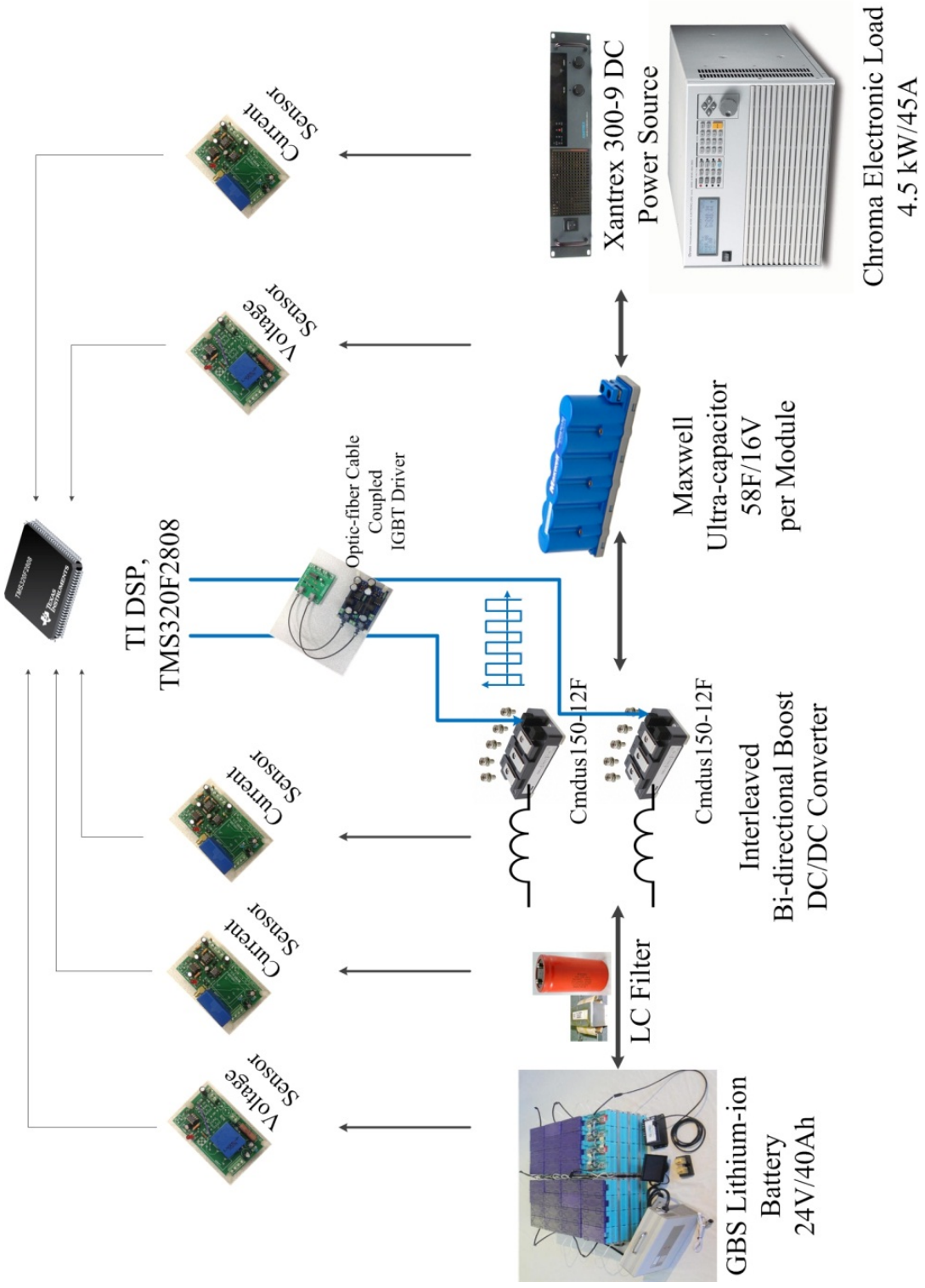

Figure 4-3 Components of the HESS Prototype

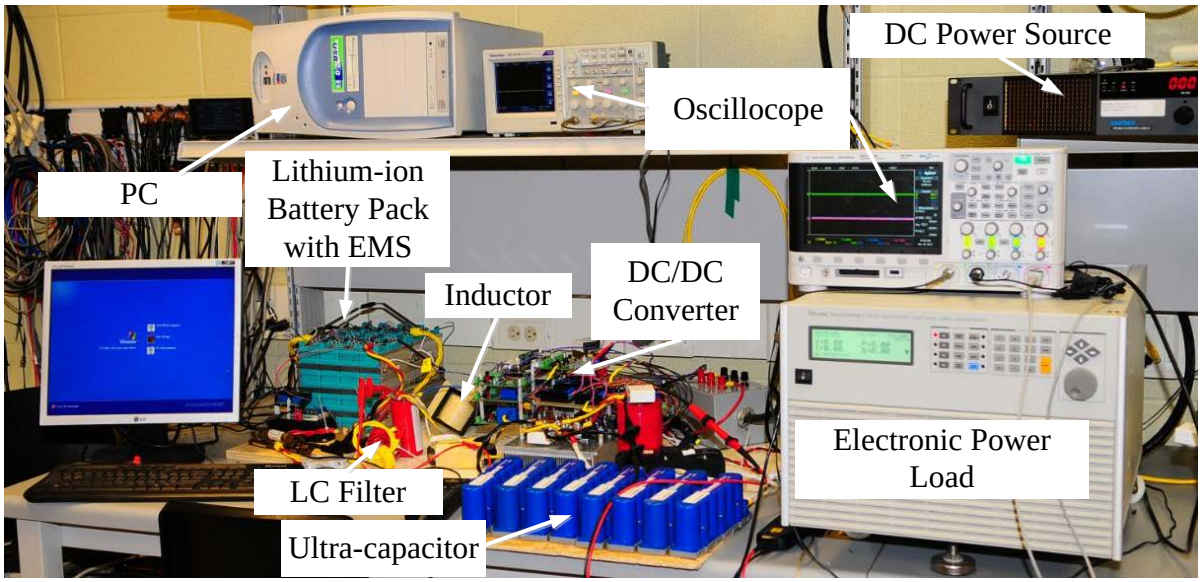

Figure 4-4 Completed HESS prototype

Table 4-3 Design specifications of the HESS prototype

Voltage range of DC/DC converter, low-voltage side	20V ~ 50V
Voltage range of DC/DC converter, high-voltage side	50V ~ 80V
Battery charging/discharging (negative/positive) current	-15A ~ 60A (-0.375C ~ 1.5C)
Current range in each boost inductor	-10A ~ +30A
Inductance of each boost inductor	500uH, 460uH
LC filter	50μH, 1mF
Capacitor on DC bus	2.4mF
Voltage sensor input voltage range	10V ~ 80V
Current sensor input current range	-60A ~ +60A
IGBT Switches	Cm150dus-12F
Switching frequency	20kHz

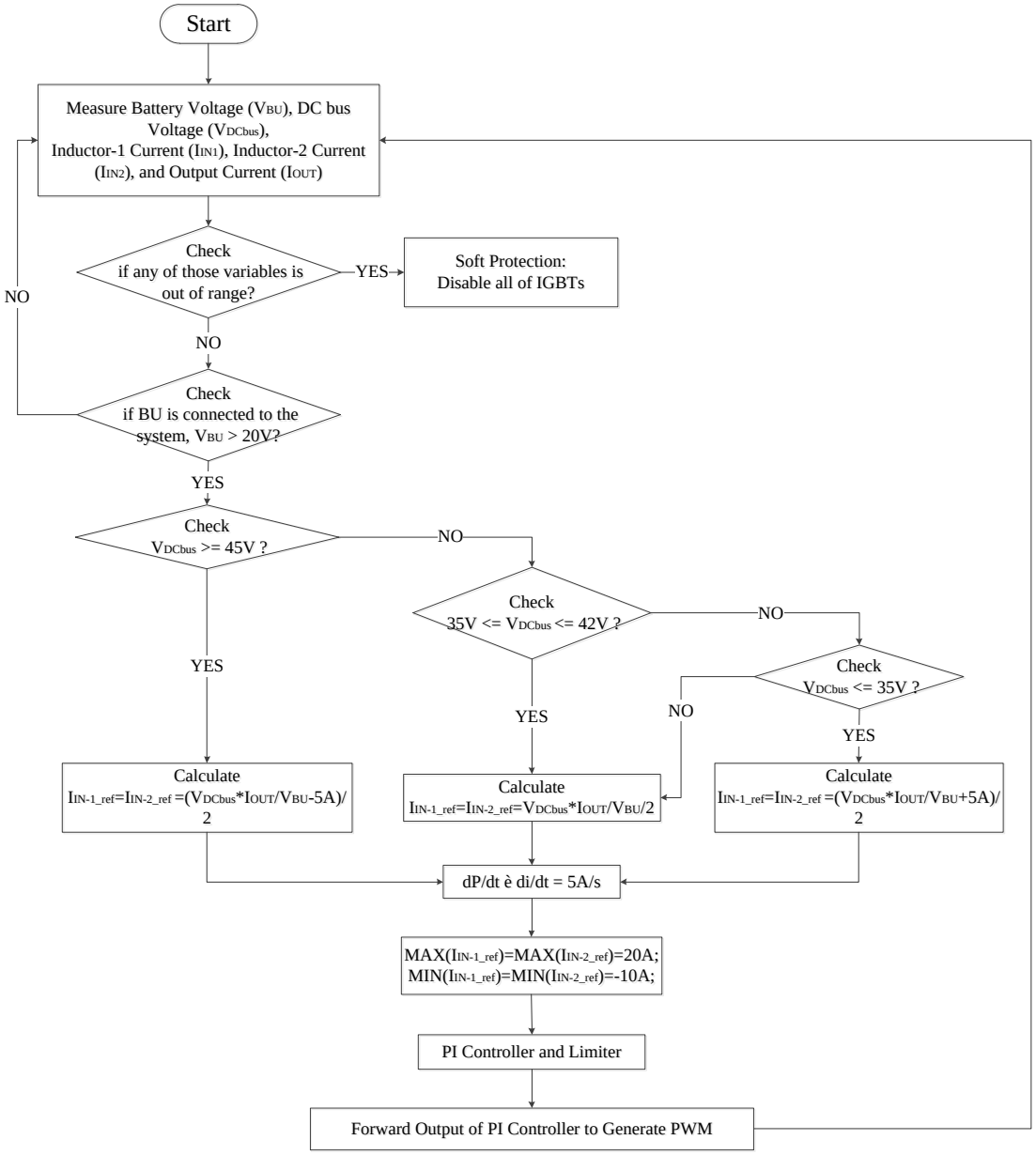

Figure 4-5 Flow diagram of HESS power management

4.3 Experiment results versus simulation results

In this section, experiment results regarding interleaved converter, HESS test setup, HESS under hard test conditions, and HESS on a designed drive cycle are discussed. Lithium-ion battery pack rated at 25.8V is connected on the low-voltage side. UC voltage is limited between 30V and 45V. BU will charge UC if DC bus voltage drops below 30V and UC will feed energy back to BU if DC bus voltage exceeds 45V. Maximum rate of rise of battery charge/discharge power is set to 30W/s.

4.3.1 Current ripple cancelation and power sharing by interleaved DC/DC converter

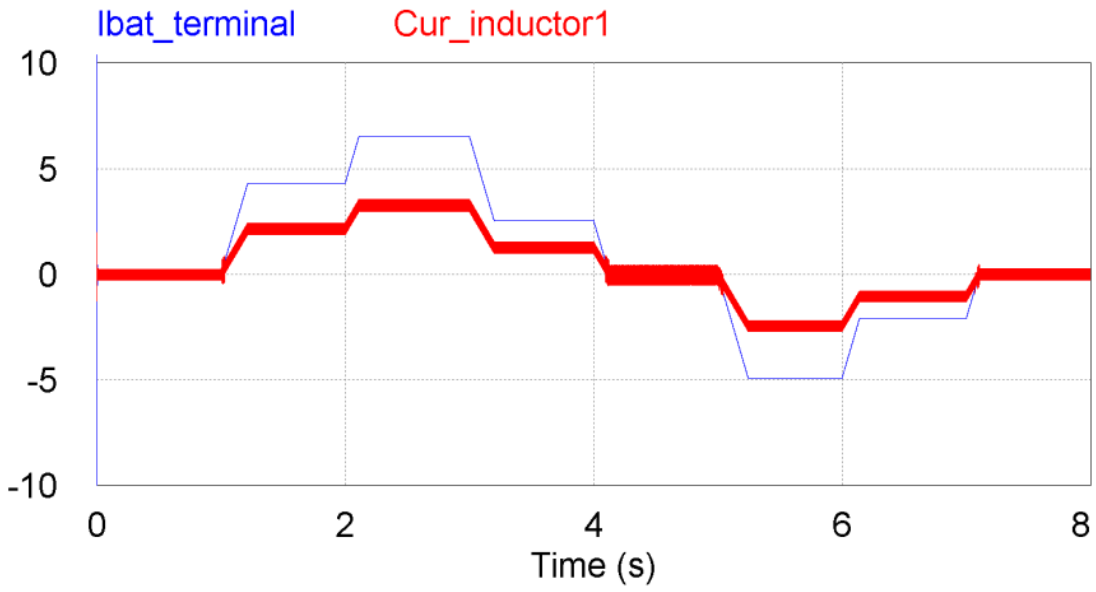

Figure 4-6 Simulation Results: Battery current (blue) and inductor current (red)

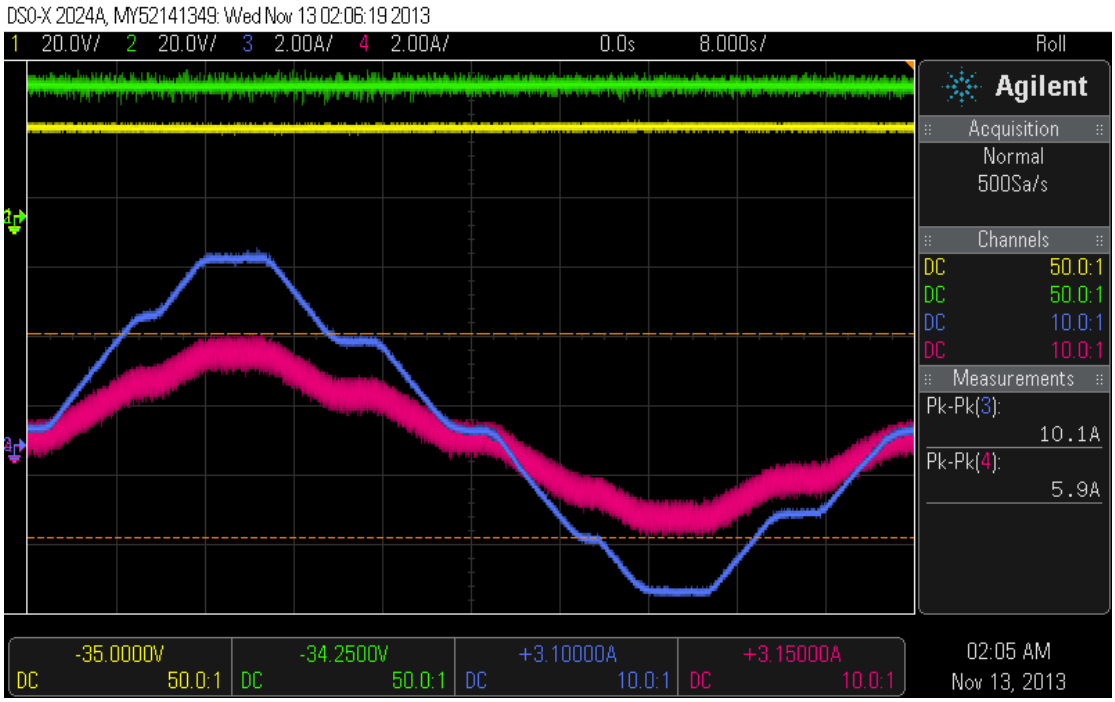

Figure 4-7 Experimental Results: Battery current (blue) and inductor current (pink)

Figures 4-6 and 4-7 demonstrate current ripple cancelation by interleaved DC/DC converter. The waveform in blue represents the battery discharging current, and the waveform in red is the current in one inductor. The local average (average per switching period) of one inductor current is half of the local average of battery current, implying that power from BU is shared by the two bi-directional buck-boost converters. Also, thanks to the interleaved structure, battery is protected from high-frequency current ripple, as shown by the blue waveform.

4.3.2 HESS tested by test setups based on DC motor and controllable power load

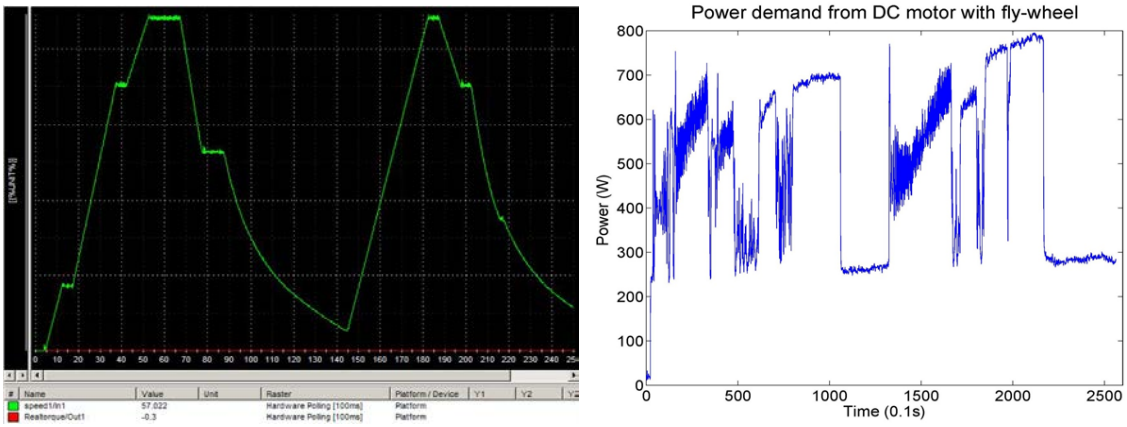

Figure 4-8 (a) Designed drive cycle for DC motor-based test setup; (b) Power profile of DC motor on the drive cycle

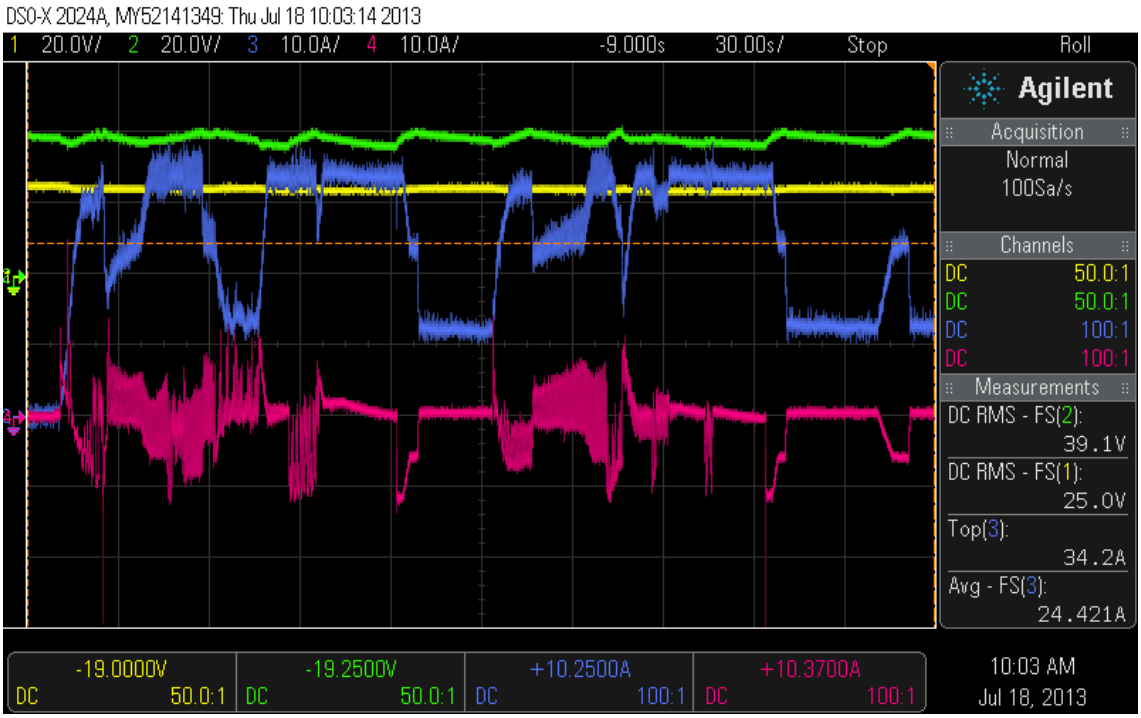

Figure 4-9 Experimental Results for DC motor-based test setup using the designed drive cycle: BU discharging current (blue); UC discharging current (pink); BU terminal voltage (yellow); DC-bus voltage (green)

HESS performance was tested using the DC motor-based test setup shown in Figure 4-1. The speed of the DC motor is controlled to follow the green waveform in Figure 4-8(a). Figure 4-8(b) is the corresponding power profile during 250 seconds. BU and UC discharging currents are shown in Figure 4-9 in blue and pink, respectively. Data representing power in Figure 4-8(b) was imported to the programmable power load. HESS was then connected to controllable power load as the test setup. Experimental results for this case are shown in Figure 4-10. The similarities between the two sets of results given in Figure 4-9 and Figure 4-10 shows the feasibility of using a controllable power load instead of DC motor-based system as HESS test setup.

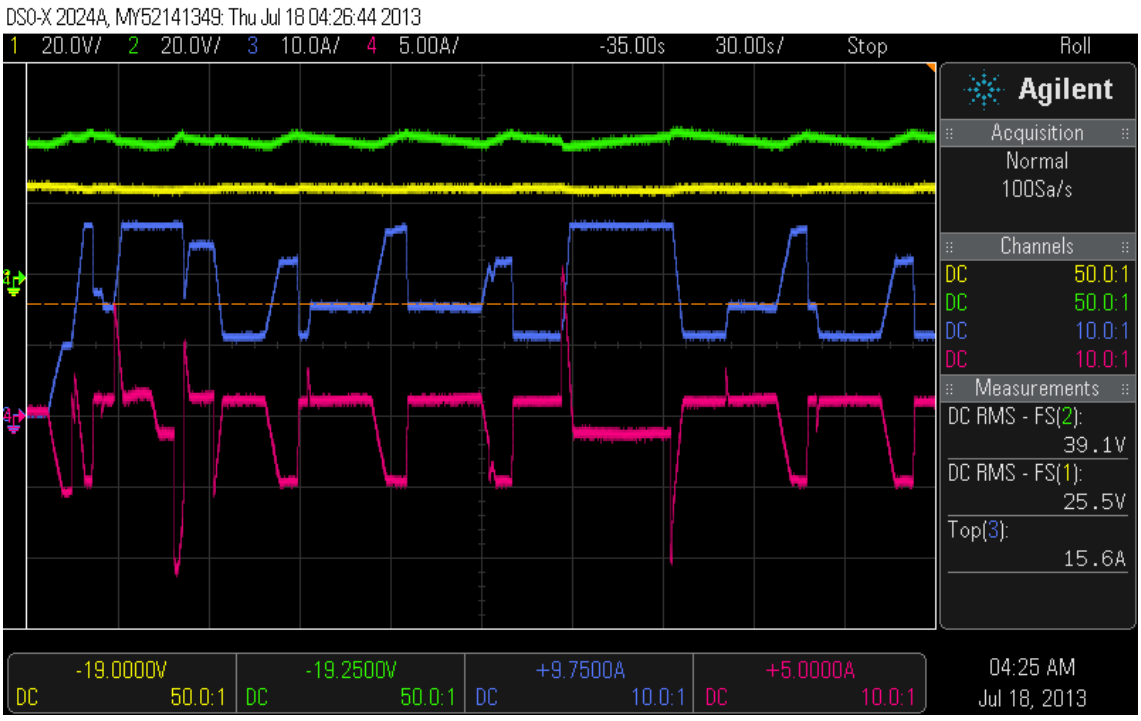

Figure 4-10 Experimental Results for controllable power load emulating DC motor using the designed drive cycle: BU discharging current (blue); UC discharging current (pink); BU terminal voltage (yellow); DC-bus voltage (green)

4.3.3 HESS tested under hard conditions

In real-life situation, the power profile imposed on HESS is not pulsed and rates of rise and fall of power are limited by laws of physics. When tested under hard conditions, the rate of change of power is chosen to be very high. If HESS performs well under hard conditions, it will certainly perform well under less severe conditions. Figure 4-11 shows a power profile with step changes. During the 15-second period, controllable power load is absorbing power from HESS in the following sequence: 0 to 300W to 600W to 200W to 0 to -150W to -300W to -100W to 0.

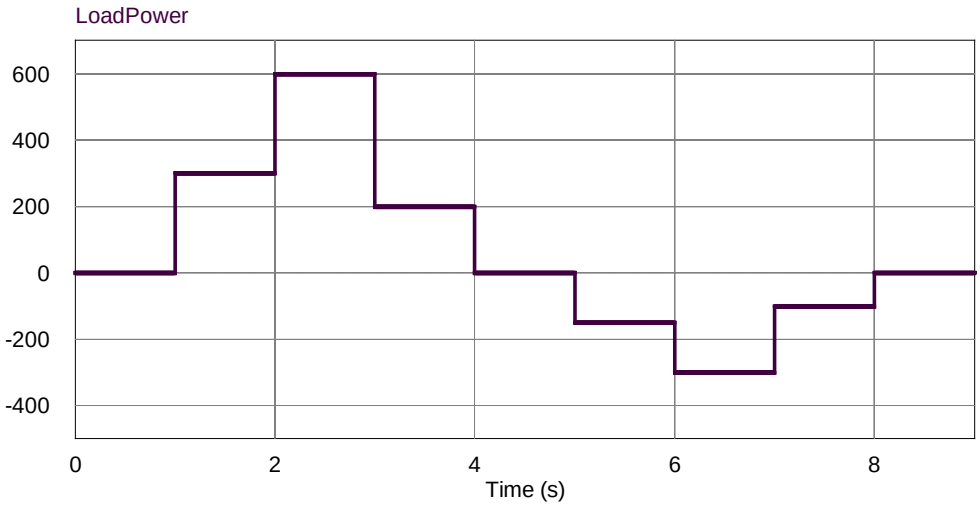

Figure 4-11 Designed power profile for HESS testing under hard conditions

As shown in Figure 4-12 and Figure 4-13, the battery current is not allowed to experience a maximum rate of change higher than $\frac{dP}{dt} = 30\text{W/s}$. Thus, BU is protected from fast-changing charge/discharge current by limiting battery power rate-of-change (or current rate-of-change). The remaining amount of power required by the load will be provided by the UC thanks to its characteristic of high specific power.

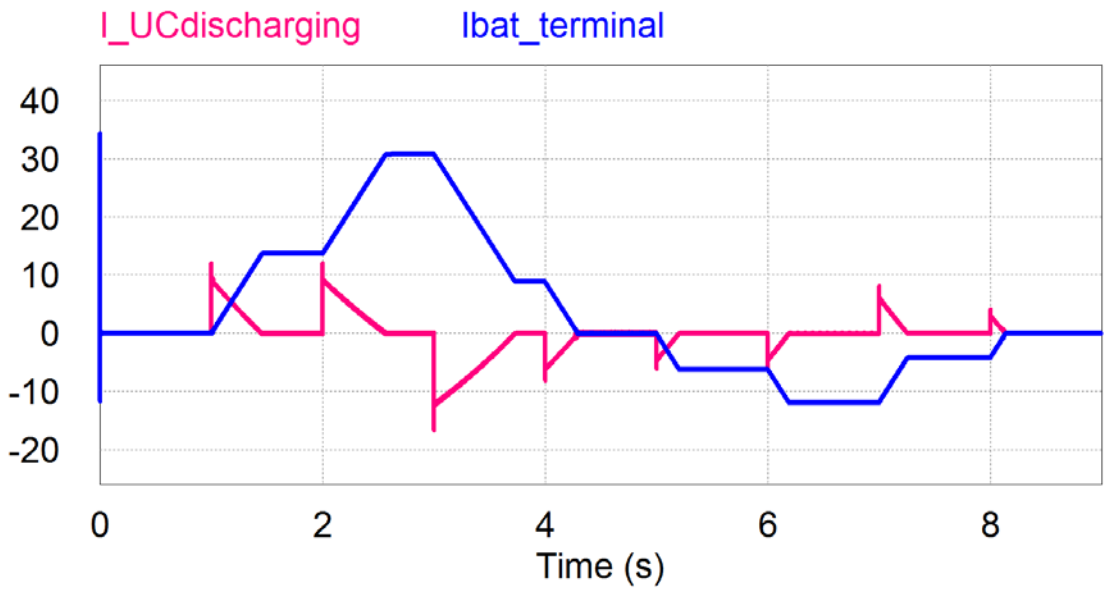

Figure 4-12 Simulation results of BU discharging current and UC discharging current under hard testing conditions

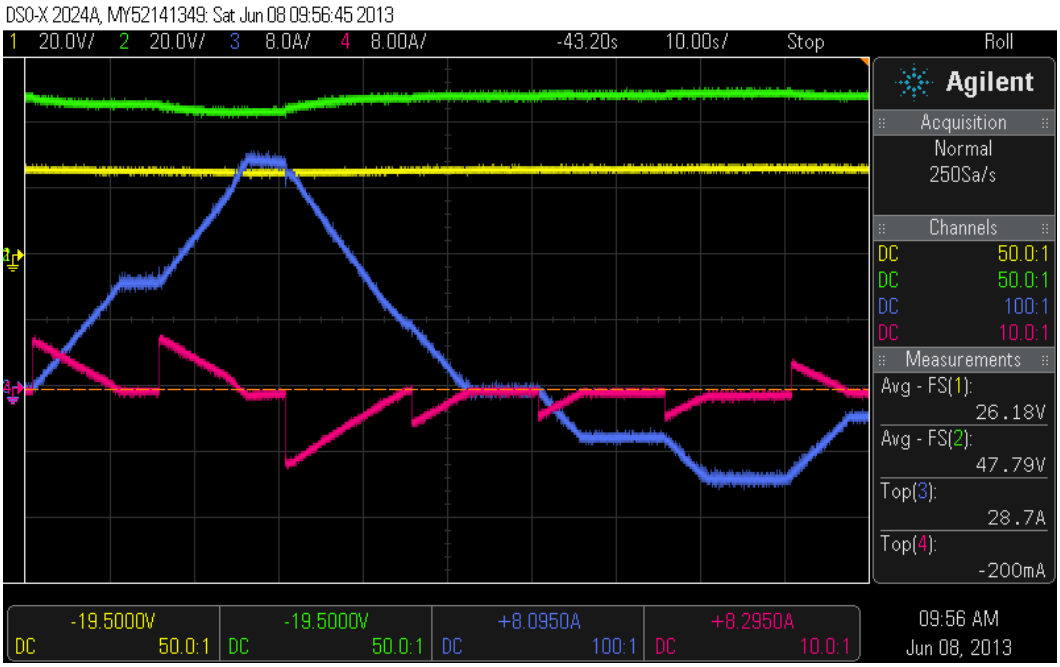

Figure 4-13 Experiment results of BU discharging current and UC discharging current under hard testing condition: BU discharging current (blue); UC discharging current (pink); BU terminal voltage (yellow); DC-bus voltage (green)

4.3.4 HESS tested on a designed drive cycle

Figure 3-20 showed 189 seconds of UDDS drive cycle and the corresponding power profile for Tesla Model S. By scaling down using a scaling factor of 1/100, a new sequence of data corresponding to power is generated with maximum value of 1kW and minimum value of -250W in order to match the power level of HESS prototype. As the HESS test setup, the controllable load is programmed based on the scaled-down power profile. Figure 4-14 and Figure 4-15 show the simulation and experimental results representing BU discharge current (in blue), UC discharge current (in pink), BU voltage (in yellow) and DC bus voltage (in green). As expected, BU is under the control of the DC/DC converter, following the designed power management algorithm.

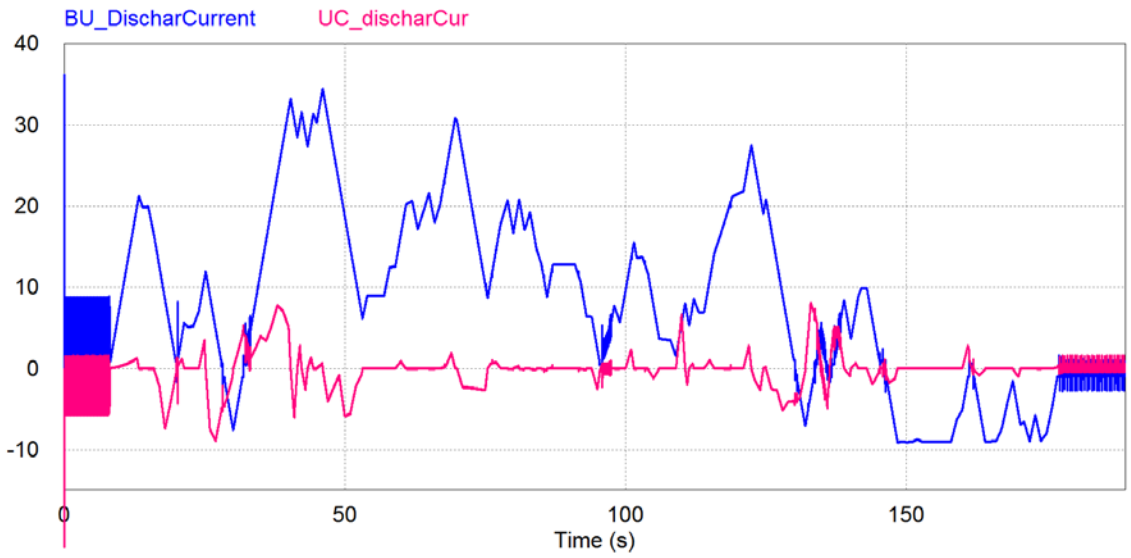

Figure 4-14 Simulation results for the designed drive cycle: BU discharging current (blue) and UC discharging current (pink)

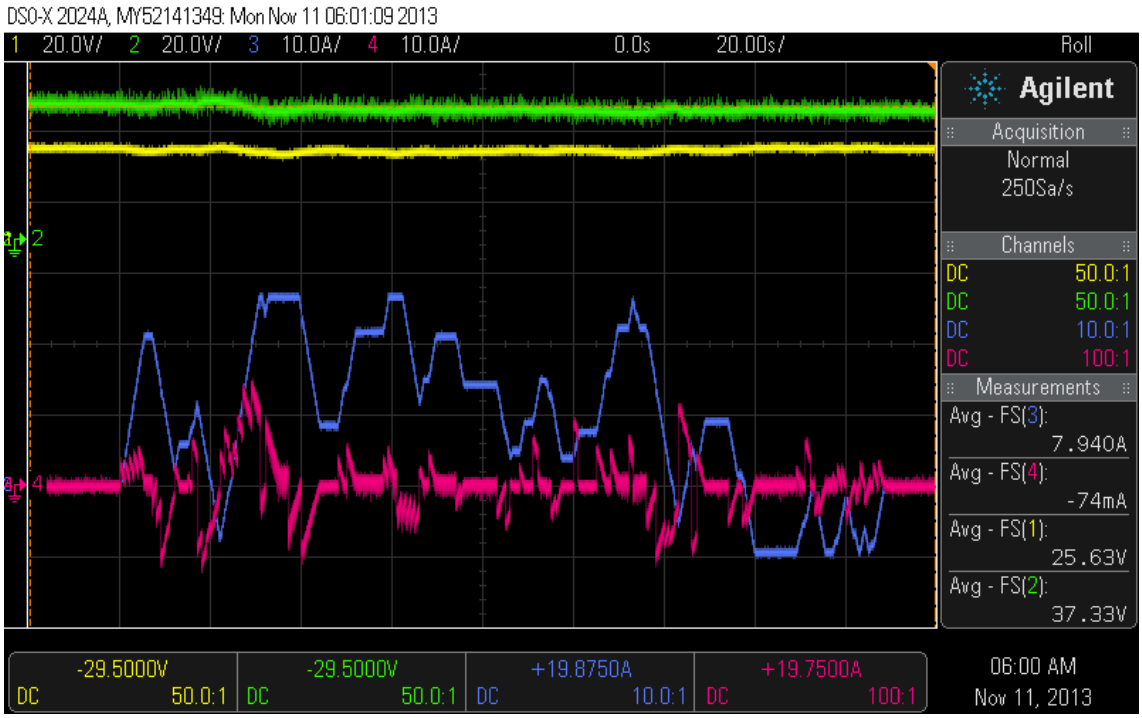

Figure 4-15 Experiment results for the designed drive cycle: BU discharging current (blue); UC discharging current (pink); BU terminal voltage (yellow) and DC-bus voltage (green)

Chapter 5

Conclusions and Future Work

5.1 Conclusion

Realization of vehicle electrification demands the development of high-performance and efficient energy storage system (ESS) for EVs and PEVs. A hybrid energy storage system (HESS), as a combination of battery and ultra-capacitor cells, is expected to take advantage of high specific energy of batteries and high specific power of ultra-capacitors. In this thesis, a HESS is designed and its capabilities are examined through simulation and experimentation.

Chapter 2 provided a comprehensive review of the technical aspects of ESS and HESS. The main components of an electrified vehicle are electric motors, energy storage devices, and power converters. The design of HESS must satisfy the requirements of traction motor drive. The interaction of lithium-ion battery and ultra-capacitor units is dictated by selection of HESS topology and power management algorithm.

In Chapter 3, HESS design procedures were presented in details. The partially-decoupled HESS topology with UC directly connected to DC bus stood out among different structures that were reviewed and evaluated, due to its relatively low cost and small size. The DC/DC converter interfacing BU and UC needed to have bi-directional power flow capability to allow energy transfer between the two energy storage devices. High

efficiency requirements for DC/DC converter leads to adoption of interleaved structure, a novel soft-switching method, as well as a bypass relay to deal with current surge. Power management algorithm is realized by the PI-based negative feedback control system. Another benefit that the selected HESS topology will bring is that the integration of HESS with on-board battery charger saves one AC/DC converter and one DC/DC converter.

Chapter 4 concentrated on the development of a scaled-down HESS prototype in laboratory. A platform for HESS performance testing was developed by combining a programmable power load and a DC source. The second part of Chapter 4 presented the experiment results for the HESS prototype, and compared these results with those obtained from simulation. The results clearly showed that the high specific power of UC could protect BU against suffering from fast-changing charge/discharge current. On the other hand, UC also improved the overall performance of ESS. Therefore, this thesis strongly proved HESS to be a promising energy storage system for an electrified vehicle.

5.2 Contributions

The main contributions of this thesis are as follows:

1) An interleaved bi-directional buck-boost DC/DC converter was designed and implemented in the lab for interfacing the battery unit and ultra-capacitor in a hybrid energy storage system for EVs and HEVs.
2) A novel capacitor-switched active snubber was introduced to the interleaved bi-directional buck-boost DC/DC converter in order to improve the overall efficiency.

5.3 Future Work

As the continuation of the work in the thesis, the inclusion of capacitor-switched snubber in the prototype is proposed. It is valuable to measure the DC/DC converter efficiency with soft-switching and compare it with the efficiency of the existing converter. A high-efficiency HESS prototype is attractive for vehicle application. Moreover, soft-switching technique allows to increase the switching frequency, thus dramatically reducing the size and cost of the inductors used in HESS. As a result, HESS can be optimized in terms of cost, weight and volume.

HESS prototype can be modified to match the requirements of the AC motor-based test setup in Table 4-2 to allow performing tests using this test setup. This AC motor-based system can emulate conditions identical to those experienced in the small-size electric vehicle “ZENN 2008”. If the HESS prototype is capable of operating with the AC motor, it is expected to be able to drive a real vehicle, when sized appropriately.

Appendix A

Table A-1 Specifications of Tesla Model S (85P)

Mass	2108 kg
Overall Length	4976mm
Width	1963mm-2187mm
Height	1435mm
Wheel Diameter (Eagle RS-A2 245/45R19)	703.58mm
Aerodynamic Drag Coefficient	0.24
Estimated Rang @ 88km/h	480km
Energy Storage	85kWh
Peak Motor Power	310kW @ 5000-8600rpm
Max Torque	600Nm @ 0-5100rpm
0-100km/h Acceleration	4.4s
Top Speed	210km/h
Gear Ratio	9.73:1
NO. of Battery Cells	~8,000
Battery Cell	Panasonic NCR18650B
Nominal Voltage	3.6V
Capacity	3350mAh (typical)
Charging Current	Std. 1625mA (0.5C)
Max Discharging Current	6700mAh (2C)
Gravimetric Energy Density	243Wh/kg
Volumetric Energy Density	676Wh/L

Appendix B

B.1 Lithium-ion Battery

One of the key components in HESS is battery. In the experiments reported in this thesis, two GBS-12V-40A lithium-ion battery modules are connected in series. Each 12V-module consists of 4 battery cells with nominal voltage of 3.2V. The battery pack has an energy management system (EMS) to monitor and balance the SoC of battery cells. The EMS includes four parts. A sensor board performs cell balancing and forwards measurements to a central processing unit (CPU); a current shunt measures battery currents up to 500A; the CPU calculates and pushes measured voltage, current, SoC and thermal information to an LCD screen. For charging BU, a compatible EMC series battery charger works under the control of CPU to achieve CC-CV charging.

B.2 Ultra-capacitor

16V-58F ultra-capacitor modules (BMOD0500 P016 B01) from Maxwell Technologies are selected for UC unit in the HESS. The modules are easy to be connected in series up to 750V and flexible to combine in parallel upon specific power and energy requirement. The UC is made up of 2 strings in which 4 modules are connected in series. Thus, voltage upper limit of UC is 64V and equivalent capacitance of UC turns out to be 29F.

B.3 IGBT Switches and Gate Drivers

IGBTs have higher power and current capabilities than MOSFETs, but they can operate at a lower switching frequency. The type of IGBTs in the HESS prototype is "CM150DUS-12F" from Powerex. The ratings are 600V, 150A and 30 kHz maximum hard switching frequency or 70 kHz maximum soft switching frequency. One IGBT module is made up of two IGBT switches with fast-recovery free-wheeling diode in anti-parallel.

IGBT drivers amplify the PWM signals produced by the DSP to turn on or turn off switches. The operation principle of IGBT drivers is presented in Figure B-1.

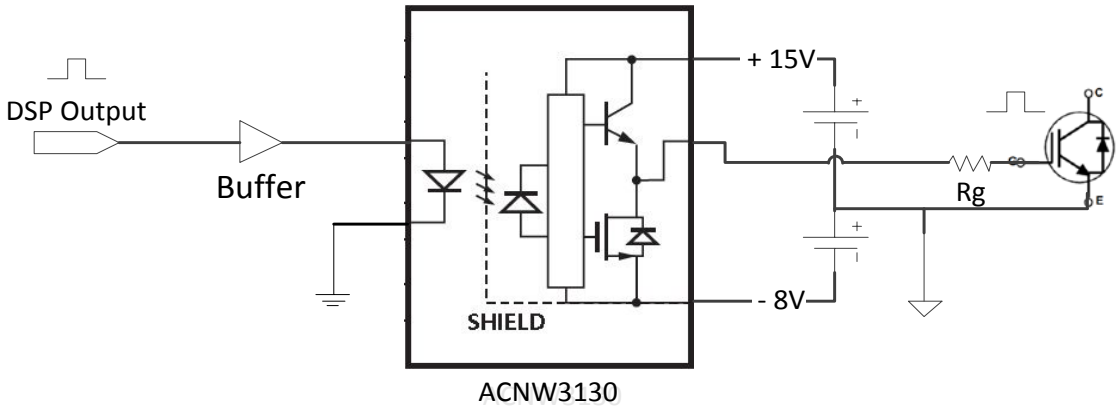

Figure B-1 IGBT Gate Driver

"ACNW3130", the IGBT gate driver optic-coupler, optically couples DSP signal with a power output stage. The buffer connects PWM signals at different voltage levels from 3.3V to 5V. The buffer also increases the drive capability of DSP I/O pin. Output of optic-coupler drives the gate of an IGBT through a gate resistor. The value of gate resistor is usually small so that stray capacitance across "gate" and "emitter" of IGBT can be quickly charged to turn on the switch. The selected value in HESS prototype is 5Ω, as mentioned in the IGBT datasheet. Figure B-2 is the photo of the designed IGBT gate driver.

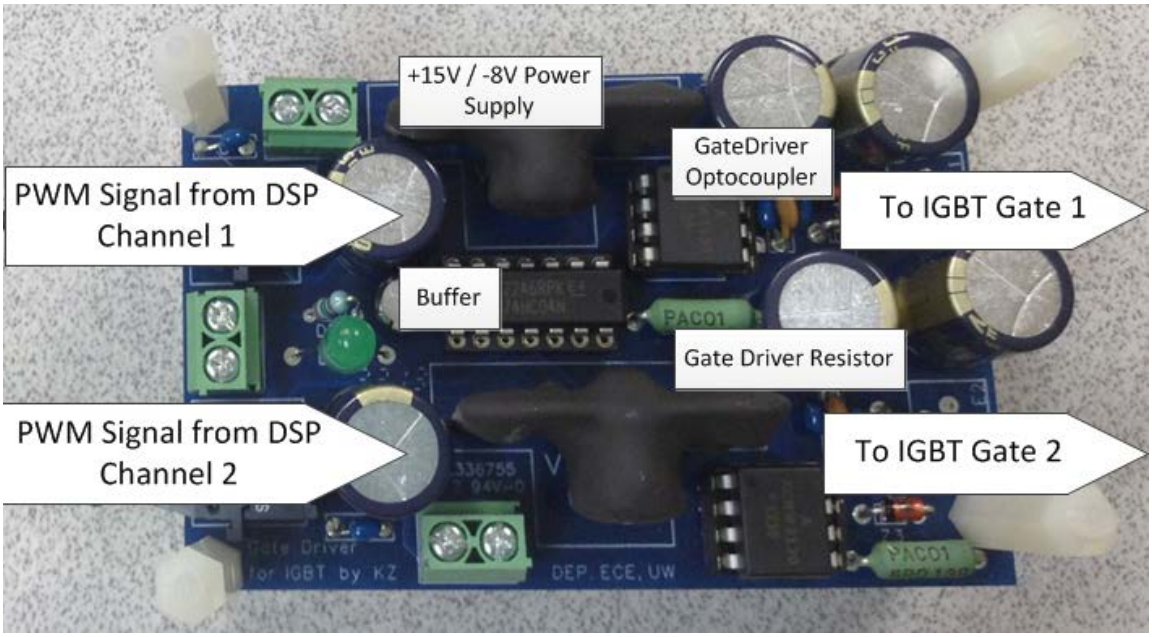

Figure B-2 Photo of IGBT Gate Driver

B.4 General Purpose Sensing Circuit (Voltage Sensor and Current Sensor)

Sensors act as “eyes” for microcontroller to see the voltage or current value in the power circuit. Different from the ideal sensors in simulation, the actual sensors should be designed with consideration of operating range and sampling accuracy. Voltage transducer and current transducer from LEM are reliable modules that are used to read voltage value and current values in circuit, and translate them to small current signals (less than 50mA) for further processing. Electricity isolation is another significant feature LEM transducers offer. It splits power ground (PG) from digital ground (DG), thus avoiding extra design for isolation. Figure B-3 presents the designed sensor schematic diagram.

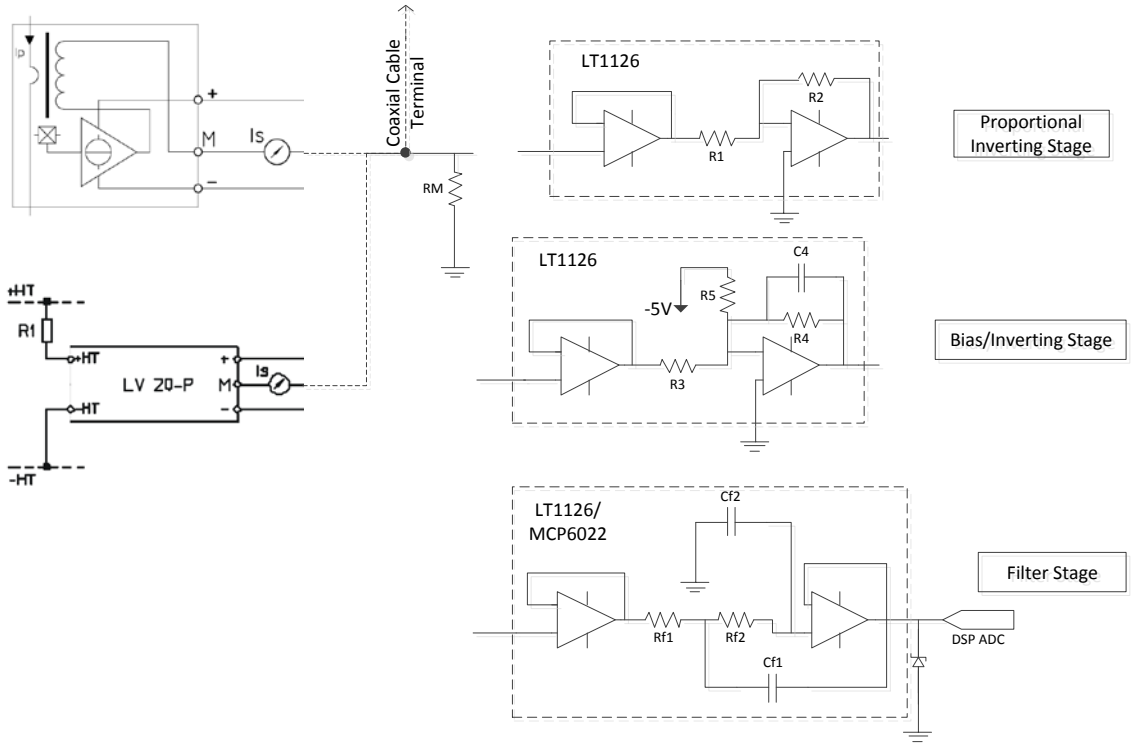

Figure B-3 Schematic Diagram of General Purpose Sensor Circuit

A high-precision resistor (0.1% tolerance) is used to transform the produced current signal to voltage signal. After that, there are three optional operational amplifiers (Op-Amp)-based circuits. The first one is called “Proportional Inverting Stage (PIS)”, whose output is sign-inverted version of the input. The ratio of R2 to R1 controls the proportional coefficient. The “Bias/Inverting Stage (BIS)” on the second adds a negative offset to the signal and inverts it. Hence, the cascade of PIS and BIS is capable of adjusting signal value domain linearly. The third stage is “Filter Stage (FS)”, prior to analogy-to-digital conversion (ADC), to limit signal’s bandwidth by an RC filter or a second-order active filter. Considering a switching frequency of 20 kHz, the cut-off frequency of the filter is set to a value between 1 kHz and 2 kHz to get rid of switching noise.

The transfer functions of PIS and BIS are as follows:

$$V_{out\_PIS} = -\frac{R2}{R1}V_{in\_PIS} \quad \text{(B.1)}$$

$$V_{out_{BIS}} = \frac{5R4}{R5} - \frac{R4}{R3}V_{in_{BIS}} \quad \text{(B.2)}$$

In order to have accurate ADC sampling results, hardware noise must be maintained at low level. The key points are:

1) A low-noise Op-Amp, $\leq 10nV/\sqrt{Hz}$ typically, should be selected. The Gain-Bandwidth Product should be 100 times higher than cut-off frequency ($\geq 100f_c$). The Slew Rate should be $\geq 2\pi V_{out_{P-P}} f_c$, where $V_{out_{P-P}}$ is the expected peak-to-peak output voltage swing.
2) The conducted noise has to be reduced by a low-pass filter prior to ADC. By-pass capacitors (ceramic capacitor and aluminum capacitor as a pair) have to be used for power supply. A ground plane has to be considered.
3) The traces on PCBs have to be shortened to minimize noise radiation. A proper shielding technique has to be implemented.

Based on the guidelines mentioned above, PCBs for voltage sensor and current sensor were designed using FreePCB software and system noise level was successfully reduced to less than 50mV (peak-to-peak). One PCB design was used for both voltage transducer and current transducer to reduce the one-time tooling cost.

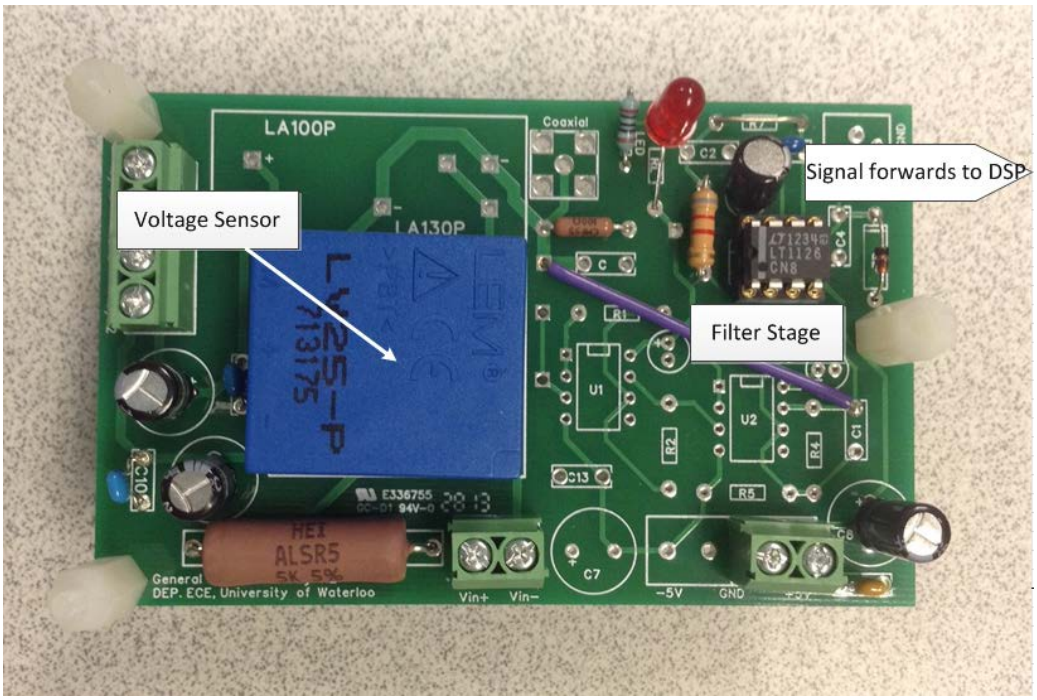

Figure B-4 Photo of PCB populated for voltage sensor

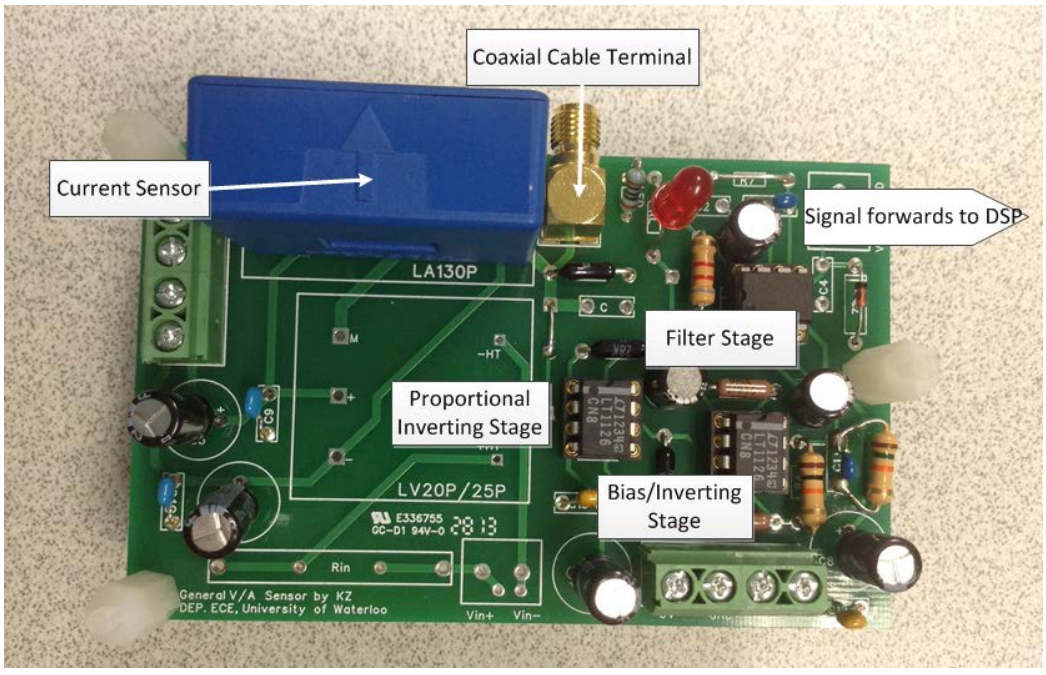

Figure B-5 Photo of PCB populated for current sensor

Figures B-4 and B-5 show voltage sensor and current sensor, respectively. The common design also brings the flexibility to users. For example, current sensor needs cascading of three op-amp stages while voltage sensor only needs filter stage. The coaxial cable terminal is provided for applications where the sensor is located far away from ADC. Coaxial cable is an excellent way of transmitting a small current signal with grounded shield.

Voltage sensor and current sensor components for HESS application are listed in Table B-2.

Table B-2 Voltage Sensor and Current Sensor Components

	Voltage Sensor	Current Sensor
Transducer Type	LV20-P, LV25-P	LA100-P
Operating range	10V-70V to 0V-3V	-100A-100A to 0-3V
Op-Amp	LT1126/MCP6022	LT1126, MCP6022
Component values	$RM = 100\Omega, 0.1\%$ $R_{in} = 5k$ $R_1 = R_2 = 28k$ $R_{f2} = 8.2k, C_{f2} = 10nF$ $C_{by-pass1} = 10uF$ $C_{by-pass2} = 220pF$	$RM = 100\Omega, 0.1\%$ $R_1 = R_2 = 28k$ $R_3 = R_5 = 20k$ $R_4 = 6k$ $R_{f2} = 8.2k, C_{f2} = 10nF$ $C_{by-pass1} = 10uF$ $C_{by-pass2} = 220pF$

B.5 Optic-fiber Connectors

DSP processes electrical signals which are of very low power. IGBT drivers amplify low power signals (in milliwatts) to high power pulses (in watts). Any tiny energy oscillation in IGBT drivers leads to high system noise in control circuit of HESS, as discovered in experiment, shown in Figure B-7. Coupled system noise made it very hard for DSP to read signals from sensors accurately, causing the failure of HESS operation.

One practical solution is using optical fiber cable for data transfer between DSP and IGBT drivers, as shown in Figure B-8.The DSP output is connected to IGBT driver through a system composed of an optical fiber transmitter, an optical fiber cable and an optical fiber receiver. The electrical signal is converted to light signal and transferred in one direction. Therefore, HESS control circuit will not couple with noise from IGBT drivers. The optical fiber cable can be long enough to meet any requirement imposed by experimental setup without electro-magnetic interference considerations. However, optical fiber cable method only works with digital signal because the light has only two states, on or off.

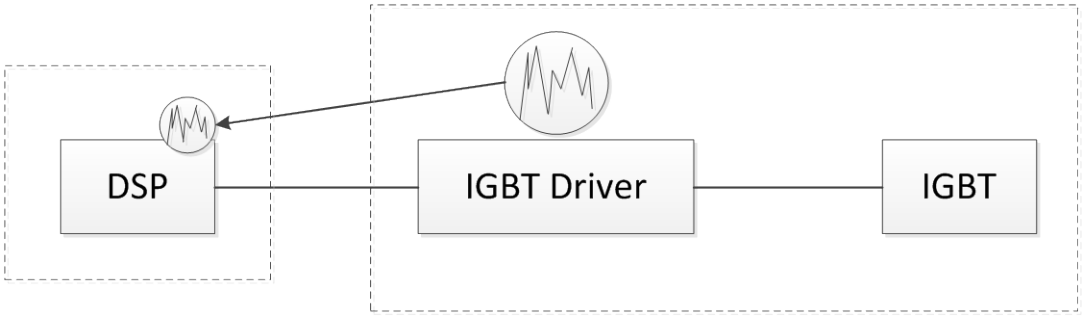

Figure B-7 Circuit Noise Problem

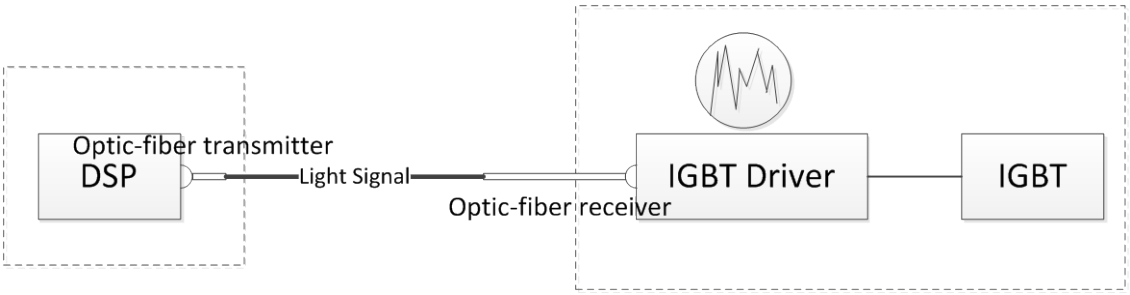

Figure B-8 Optic-fiber to Isolate Circuit Noise

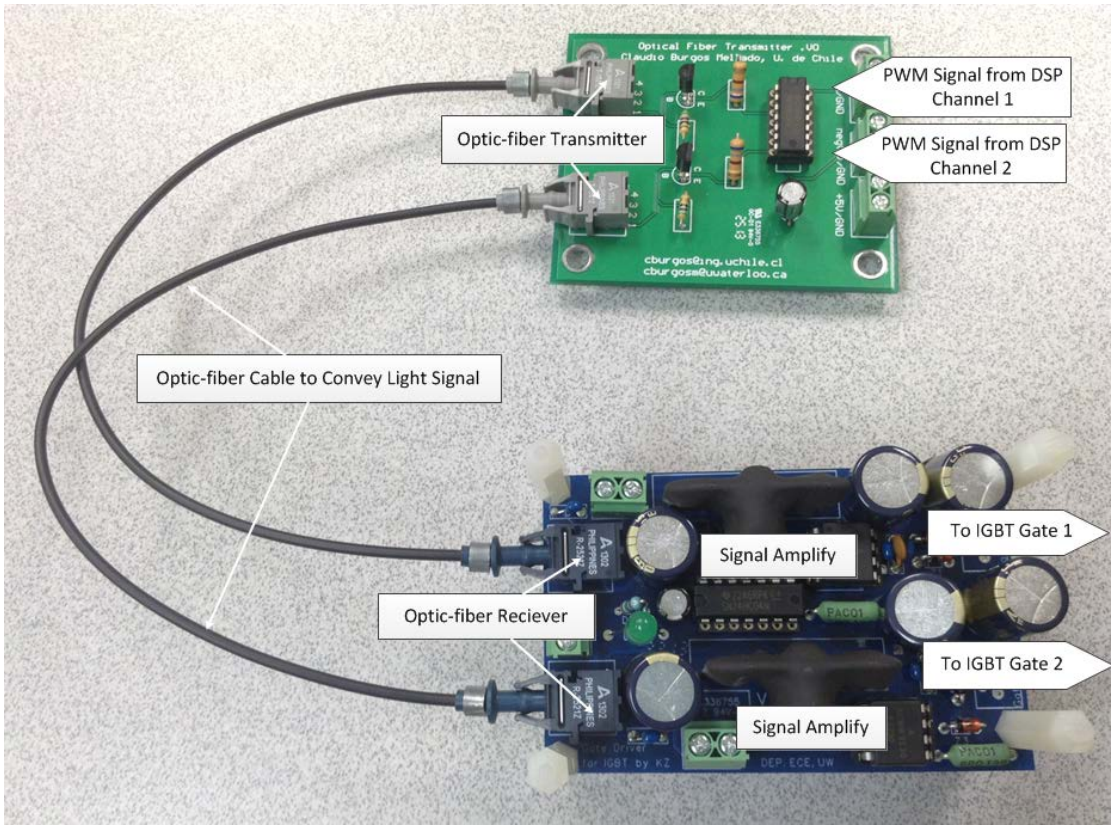

Figure B-9 Photo of System of Data Transfer between DSP and IGBT Driver via Light to Isolate Circuit Noise

B.6 DSP Microcontroller

Texas Instruments TMS320F2808 is a 32-bit digital signal processor (DSP) with high-speed computing capability of 100MHz. The DSP provides16 channels of pulse width modulation (PWM) outputs, 16 channels of 12-bit analogy-to-digital conversion (ADC) inputs, and 35 channels of general purpose inputs/outputs (GPIOs). The TMS320F2808 experimental kit has a user-friendly docking station that makes it easy for use with the lab prototype.

B.7 Inductors and Capacitors

There were a number of DC inductors in the lab with the following specifications: 100uH/40A, 360uH/40A, DC, 500uH/45A, DC, and 1.3mH/70A. Series connection of the first two inductors gives an equivalent inductance of 460uH. Together with the 500uH/45A, DC inductor, they are going to be used for the interleaved bi-directional buck-boost converter. This is the closest one could get with the available components.

Available capacitors were electrolytic capacitors designed for high current ripples from Duracap Company. The 2.4mF, 500VDC with the current ripple limit of $\pm$ 11A was used on the DC bus for absorbing high-frequency ripples in the bidirectional current. It should be noted that ultra-capacitor cannot act as a capacitor at high frequencies despite its high capacitance at low frequencies. The 1mF, 500VDC electrolytic capacitor with current ripple limit of $\pm$ 11.7A was used for the LC filter smoothing the battery current.

B.8 IGBT Protection

IGBTs are expensive components and they are sensitive to voltage/current surge caused due to converter's malfunction. Beside software protection, a hardware protection system consisting of MOV and semiconductor fuse is in place. Metal-Oxide Varistors (MOVs) have variable resistors depending on the applied voltage. Over voltage results in low resistance of MOV that helps maintain safe voltage across the switch. Semiconductor

fuse is an effective method to protect IGBTs from over current thanks to its very fast response to the overcurrent.

Appendix C

Appendix C

C.1 Code of analog to digital conversion (ADC)

```
long int RESULT0,RESULT1,RESULT2,RESULT3;
_iq         ADC_fk_iq[5] ={
                                _IQ(0.015246163),   // Bat Voltage              ****ADC_out_iq[0]
                                _IQ(0.024948025),   // UC Voltage/DC Bus Voltage****ADC_out_iq[1]
                                _IQ(0.048855652),   // Converter Current 1      ****ADC_out_iq[2]
                                _IQ(0.048855652),   // Converter Current 2      ****ADC_out_iq[3]
                                _IQ(0.048855652),   // Load Current             ****ADC_out_iq[4]

                            }

void ADCsampling(void)
{
    long int RESULT0=0,RESULT1=0,RESULT2=0,RESULT3=0, RESULT4 = 0;

    RESULT0=AdcRegs.ADCRESULT0>>4;
    RESULT0+=AdcRegs.ADCRESULT1>>4;
    RESULT0+=AdcRegs.ADCRESULT2>>4;
    RESULT0=RESULT0/3;

    RESULT1=AdcRegs.ADCRESULT3>>4;
    RESULT1+=AdcRegs.ADCRESULT4>>4;
    RESULT1+=AdcRegs.ADCRESULT5>>4;
    RESULT1=RESULT1/3;

    RESULT2=AdcRegs.ADCRESULT6>>4;
    RESULT2+=AdcRegs.ADCRESULT7>>4;
    RESULT2+=AdcRegs.ADCRESULT8>>4;
    RESULT2=RESULT2/3;

    RESULT3=AdcRegs.ADCRESULT9>>4;
    RESULT3+=AdcRegs.ADCRESULT10>>4;
    RESULT3+=AdcRegs.ADCRESULT11>>4;
    RESULT3=RESULT3/3;

    RESULT4=AdcRegs.ADCRESULT12>>4;
    RESULT4+=AdcRegs.ADCRESULT13>>4;
    RESULT4+=AdcRegs.ADCRESULT14>>4;
    RESULT4+=AdcRegs.ADCRESULT15>>4;
    RESULT4=RESULT4/4;

    ADC_out_iq[0]=_IQmpyIQX(_IQ18(RESULT0),18,ADC_fk_iq[0],19);     // Voltage Input - Battery Voltage
    ADC_out_iq[0]+=_IQ(0.471995767);

    ADC_out_iq[1]=_IQmpyIQX(_IQ18(RESULT1),18,ADC_fk_iq[1],19);     // Voltage Output - DC Bus Voltage
    ADC_out_iq[1]+=_IQ(0.51247401);

    ADC_out_iq[2]=_IQmpyIQX(_IQ18(RESULT2),18,ADC_fk_iq[2],19);     // Current Input 1
    ADC_out_iq[2]+=_IQ(-107.294917);

    ADC_out_iq[3]=_IQmpyIQX(_IQ18(RESULT3),18,ADC_fk_iq[3],19);     // Current Input 2
    ADC_out_iq[3]+=_IQ(-106.8255766);

    ADC_out_iq[4]=_IQmpyIQX(_IQ18(RESULT4),18,ADC_fk_iq[4],19);     // Current Output
    ADC_out_iq[4]+=_IQ(-106.7003819);

    return;
}
```

C.2 Code of power management

```
if((ADC_out_iq[1]<=_IQ(35))||(Flag_UCapH==0))
{
    Flag_UCapH=0;
    UCapC_RamUp_iq = UCapC_RamUp_iq + _IQ(0.0001);
    if(UCapC_RamUp_iq >= _IQ(10) )
    {
        UCapC_RamUp_iq = _IQ(10);
    }
}
if(((ADC_out_iq[1]>=_IQ(42))&&(UCapC_RamUp_iq>_IQ(0)))||(Flag_UCapH==1))
{
    Flag_UCapH=1;
    UCapC_RamUp_iq = UCapC_RamUp_iq + _IQ(-0.001);
    if(UCapC_RamUp_iq <= _IQ(0) )
    {
        UCapC_RamUp_iq = _IQ(0);
    }
}
if (ADC_out_iq[1]>=_IQ(45))
{
    UCapC_RamUp_iq = UCapC_RamUp_iq + _IQ(-0.001);
    if(UCapC_RamUp_iq <= _IQ(-5) )
    {
        UCapC_RamUp_iq = _IQ(-5);
    }
}


Out_Power_iq = _IQmpy(Out_Voltage_iq,Out_Current_iq);              //Load Power
In_Power_Ref_iq = Out_Power_iq;                                    //Battery Power reference
In_Current_Ref_iq = _IQdiv(In_Power_Ref_iq, In_Voltage_iq);        //Battery Current reference

Bat_Power_Ref_iq[1]=In_Power_Ref_iq;                               //  dp/dt limiter
if(Bat_Power_Ref_iq[1]>=Bat_Power_Ref_iq[0]) /// "+" sign
{
    if((Bat_Power_Ref_iq[1] - Bat_Power_Ref_iq[0])>=_IQ(0.005))    /// 10Watt/Sec*50us=0.0005
    {
        Bat_Power_Ref_dpdt_iq= Bat_Power_Ref_iq[0] + _IQ(0.005);   /// 30Watt/Sec*50us=0.0015
        Bat_Power_Ref_iq[0] = Bat_Power_Ref_dpdt_iq;
    }
    else
    {
        Bat_Power_Ref_dpdt_iq= Bat_Power_Ref_iq[1];
        Bat_Power_Ref_iq[0] = Bat_Power_Ref_dpdt_iq;
    }
}
if(Bat_Power_Ref_iq[1] < Bat_Power_Ref_iq[0])  /// "-" sign
{
    if((Bat_Power_Ref_iq[0] - Bat_Power_Ref_iq[1])>=_IQ(0.005))
    {
        Bat_Power_Ref_dpdt_iq= Bat_Power_Ref_iq[0] - _IQ(0.005);
        Bat_Power_Ref_iq[0] = Bat_Power_Ref_dpdt_iq;
    }
    else
    {
        Bat_Power_Ref_dpdt_iq= Bat_Power_Ref_iq[1];
        Bat_Power_Ref_iq[0] = Bat_Power_Ref_dpdt_iq;
    }
}
In_Current_Ref_dpdt_iq_1 = _IQdiv(Bat_Power_Ref_dpdt_iq, In_Voltage_iq);
In_Current_Ref_dpdt_iq = In_Current_Ref_dpdt_iq_1 + UCapC_RamUp_iq;
if(In_Current_Ref_dpdt_iq>=_IQ(30))
{
    In_Current_Ref_dpdt_iq = _IQ(30);        //set maximum battery discharge current at 30A
}
if(In_Current_Ref_dpdt_iq<=_IQ(-20))
{
    In_Current_Ref_dpdt_iq = _IQ(-20);       //set maximum battery charge current at 20A
}
In_Current_Ref_dpdt_iq = _IQmpy(In_Current_Ref_dpdt_iq, _IQ(0.5));
//Current is shared by DC/DC converters
```

C.3 Code of PI controller

```
   Bat_ie_iq = In_Current_Ref_dpdt_iq - ADC_out_iq[2];
   Bat_i_ki_iq[1] = Bat_i_ki_iq[0]+_IQmpyIQX(Bat_i_kiTs_iq,28, Bat_ie_iq,19);      // Calulate I
   Bat_i_PI_iq = Bat_i_ki_iq[1]+_IQmpyIQX(Bat_i_kp_iq,25,Bat_ie_iq,19);           // Calculate PI
   Bat_i_ki_iq[0] = Bat_i_ki_iq[1]; // "1" current state, "0" previous state

   Bat_pwm_iq = _IQsat(Bat_i_PI_iq,_IQ(0.95),_IQ(-0.95));
//   Bat_pwm_iq = _IQ(0.9);         // for testing

   UCMP_Bat = 1250 -  _IQmpyI32int( Bat_pwm_iq, 1250);     // Duty ratio for 1A and 1B

   BatC2_ie_iq = In_Current_Ref_dpdt_iq - ADC_out_iq[3];
   BatC2_i_ki_iq[1] = BatC2_i_ki_iq[0]+_IQmpyIQX(BatC2_i_kiTs_iq,28, BatC2_ie_iq,19);      // Calulate I
   BatC2_i_PI_iq = BatC2_i_ki_iq[1]+_IQmpyIQX(BatC2_i_kp_iq,25,BatC2_ie_iq,19);           // Calculate PI
   BatC2_i_ki_iq[0] = BatC2_i_ki_iq[1]; // "1" current state, "0" previous state

   BatC2_pwm_iq = _IQsat(BatC2_i_PI_iq,_IQ(0.95),_IQ(-0.95));
//   BatC2_pwm_iq = _IQ(0.9);       // for testing

   UCMP_BatC2 = 1250 -  _IQmpyI32int( BatC2_pwm_iq, 1250);     // Duty ratio for 1A and 1B

   EALLOW;
   GpioCtrlRegs.GPAMUX1.bit.GPIO0  =1;     //EPWM1A
   GpioCtrlRegs.GPAMUX1.bit.GPIO2  =1;     //EPWM2A

   GpioCtrlRegs.GPAMUX1.bit.GPIO4  =1;     //EPWM1A
   GpioCtrlRegs.GPAMUX1.bit.GPIO6  =1;     //EPWM2A
   EDIS;

   EPwm1Regs.CMPA.half.CMPA = UCMP_Bat;        // Setting comparison value for 1A
   EPwm2Regs.CMPA.half.CMPA = UCMP_Bat;        // Setting comparison value for 1B

   EPwm3Regs.CMPA.half.CMPA = UCMP_BatC2;      // Setting comparison value for 1B  gpio 04
   EPwm4Regs.CMPA.half.CMPA = UCMP_BatC2;      // Setting comparison value for 1B  gpio 06
```

References

References

[1] M. Valentine-Urbschat and W. Bernhart, “Powertrain 2020 – The Future Drives Electric”, 2009 [Online]. Available: http://www.rolandberger.at/media/pdf/Roland_Berger_Powertrain_2020_20110215.pdf

[2] K. Gyimesi, and R. Viswanatban, “The shift to electric vehicles”, I. B. M. Global Business Services Executive Report, 2011 [Online]. Available: http://www-935.ibm.com/services/us/gbs/thoughtleadership/ibv-electric-vehicle.html

[3] R. Mabro, “Oil in the 21st century: issues, challenges and opportunities,” Oxford University Press, 2006.

[4] K. B. Mikkelsen, “Design and Evaluation of Hybrid Energy Storage Systems for Electric Powertrains”, Master of Applied Science Thesis, University of Waterloo, 2010.

[5] S. M. Lukic, J. Cao, R. C. Bansal, F. Rodriguez, and A. Emadi, “Energy Storage Systems for Automotive Applications,” *IEEE transactions on industrial electronics*, vol. 55, no. 6, pp. 2258–2267, 2008.

[6] Y. Gurkaynak, A. Khaligh, A. Emadi, “State of the Art Power Management Algorithms for Hybrid Electric Vehicles,” *Vehicle Power and Propulsion Conference*, 2009, pp. 388–394, 2009.

[7] J. Bauman, M. Kazerani “An Analytical Optimization Method for Improved Fuel Cell – Battery – Ultracapacitor Powertrain,” *IEEE Transactions on Vehicular Technology*, vol. 58, no. 7, pp. 3186–3197, 2009.

[8] Tesla Motors Inc., “Supercharger of Tesla Motors”, 2012 [Online]. Available: http://www.teslamotors.com/en_CA/supercharger.

[9] US. Environmental Protection Agency, “Dynamometer Drive Schedules, Testing and Measuring Emissions,” [Online]. Available: http://www.epa.gov/nvfel/testing/dynamometer.htm

[10] P. S. Mohanbhai and P. P. Mohanbhai, “Effective power and energy management for the dual source hybrid electric vehicle based on the measured drive cycle,” *2012 IEEE 5th India Int. Conf. Power Electron.*, pp. 1–6, Dec. 2012.

[11] S. G. Wirasingha, R. Gremban, A. Emadi, “Source-to-Wheel (STW) Analysis of Plug-in Hybrid Electric Vehicles,” *IEEE Transactions on Smart Grid*, vol. 3, no. 1, pp. 316–331, 2012.

[12] “The Australian Electric Vehicle Asn.” [Online]. Available: http://forums.aeva.asn.au/forums/why-1-f_topic1984.html.

[13] A. Khaligh, Z. Li, “Battery , Ultracapacitor , Fuel Cell , and Hybrid Energy Storage Systems for Electric , Hybrid Electric , Fuel Cell , and Plug-In Hybrid Electric Vehicles : State of the Art,” *IEEE Transactions on Vehicular Technology*, vol. 59, no. 6, pp. 2806–2814, 2010.

[14] J. Cao, A. Emadi “A New Battery / UltraCapacitor Hybrid Energy Storage System for Electric , Hybrid , and Plug-In Hybrid Electric Vehicles,” *IEEE Transactions on Power Electronics*, vol. 27, no. 1, pp. 122–132, 2012.

[15] M. Chen, G. A. Rinc, “Accurate Electrical Battery Model Capable of Predicting Runtime and I – V Performance,” *IEEE Transactions on Energy Conversion*, vol. 21, no. 2, pp. 504–511, 2006.

[16] T. Kim, W. Qiao, “A Hybrid Battery Model Capable of Capturing Dynamic Circuit Characteristics and Nonlinear Capacity Effects,” *IEEE Power and Energy Society General Meeting*, pp. 1–9, 2012.

[17] F. Rafik, H. Gualous, R. Gallay, a. Crausaz, and a. Berthon, “Frequency, thermal and voltage supercapacitor characterization and modeling,” *Power Electronics and Motion Control Conference, 2006. IPEMC 2006. CES/IEEE 5th International*, vol. 165, no. 2, pp. 928–934, Mar. 2007.

[18] N. Wong, K. Zhuge, M.Kazerani, “Design of a Two-Stage Level-Two Bidirectional On-Board Battery Charger for Plugin Vehicles,” *IEEE Transportation Electrification Conference and Expo (ITEC)*, pp. 1-5, 2013.

[19] J. Cao, N. Schofield, and A. Emadi, “Battery balancing methods: A comprehensive review,” *Vehicle Power and Propulsion Conference, 2008. VPPC '08. IEEE*, pp. 1–6, Sep. 2008.

[20] P. A. Cassani, and S. S. Williamson, “Feasibility Analysis of a Novel Cell Equalizer Topology for Plug-In Hybrid Electric Vehicle Energy-Storage Systems,” *IEEE Transactions on Vehicular Technology*, vol. 58, no. 8, pp. 3938–3946, 2009.

[21] P. A. Cassani, S. Member, and S. S. Williamson, “Design , Testing , and Validation of a Simplified Control Scheme for a Novel Plug-In Hybrid Electric Vehicle Battery Cell Equalizer,” IEEE Transactions on Industrial Electronics, vol. 57, no. 12, pp. 3956–3962, 2010.

[22] A. Ostadi, M. Kazerani, and S.-K. Chen, “Hybrid Energy Storage System (HESS) in vehicular applications: A review on interfacing battery and ultra-capacitor units,” *2013 IEEE Transportation Electrification Conference and Expo*, pp. 1–7, Jun. 2013.

[23] R. Carter, A. Cruden, and P. J. Hall, “Optimizing for Efficiency or Battery Life in a Battery/Supercapacitor Electric Vehicle,” *IEEE Transactions on Vehicular Technology*, vol. 61, no. 4, pp. 1526–1533, May 2012.

[24] A. Kuperman, I. Aharon, S. Malki, and A. Kara, “Design of a Semiactive Battery-Ultracapacitor Hybrid Energy Source,” *IEEE Transaction on Power Electronics*, vol. 28, no. 2, pp. 806–815, Feb. 2013.

[25] J. Bauman, M. Kazerani, “A Comparative Study of Fuel-Cell – Battery , Fuel-Cell – Battery – Ultracapacitor Vehicles,” *IEEE Transactions on Vehicular Technology*, vol. 57, no. 2, pp. 760–769, 2008.

[26] M. H. Rashid, “Power Electronics, Circuits, Devices, and Applications”, Pearson/Prentice Hall, 2004.

[27] A. S. Samosir, M. Anwari, and A. H. M. Yatim, “Dynamic Evolution Control of Interleaved Boost DC-DC Converter for Fuel Cell Application,” *2010 Conf. Proc. IPEC*, pp. 869–874, Oct. 2010.

[28] N. Coruh, “A Simple And Efficient Implemantation Of Interleaved Boost Converter”, 2011 6th IEEE Conference on Industrial Electronics and Applications (ICIEA), no. Dcm, pp. 2364–2368, 2011.

[29] Powerex Inc. Power Semiconductor Solutions, “Powerex Product: CM150DUS-12F.” [Online]. Available: http://www.pwrx.com/Product/CM150DUS-12F.

[30] J. Bauman, M. Kazerani, “A Novel Capacitor-Switched Regenerative Snubber for DC / DC Boost Converters,” *IEEE Transactions on Industrial Electronics*, vol. 58, no. 2, pp. 514–523, 2011.

[31] K. Fujiwara, and H. Nomura, “A Novel Lossless Passive Snubber for Soft-switching Boost-type Converters,” *IEEE Transactions on Power Electronics*, vol. 14, no. 6, pp. 1065–1069, 1999.

[32] J. Marshall and M. Kazerani, “A Novel Lossless Snubber for Boost Converters”, *IEEE International Symposium on Industrial Electronics*, 2006.

[33] G. Ning, B. Haran, and B. N. Popov, “Capacity fade study of lithium-ion batteries cycled at high discharge rates,” *Journal of Power Sources*, vol. 117, no. 1–2, pp. 160–169, May 2003.

[34] D. Maksimovic, Rober W. Erickson, “Fundamentals of Power ELectronics - 2nd Edition,” Kluwer Academic Publishers, 2004.

[35] N. Wong, M. Kazerani, “A Review Of Bidirectional On-Board Charger Topologies For Plugin Vehicles," *25th IEEE Canadian Conference Electrical & Computer Engineering (CCECE)*, pp. 0–5, 2012.

[36] G. Su and L. Tang, “Current source inverter based traction drive for EV battery charging applications”, *Vehicle Power and Propulsion Conference (VPPC)*, pp. 1–6, Sep. 2011.